

# Structural studies of eight bright rimmed clouds in the southern hemisphere

Saurabh Sharma<sup>1</sup>, A. K. Pandey<sup>1</sup>, J. Borissova<sup>2,7</sup>, D. K. Ojha<sup>3</sup>, V. D. Ivanov<sup>4</sup>, K. Ogura<sup>5</sup>, N. Kobayashi<sup>6</sup>, R. Kurtev<sup>2,7</sup>, M. Gopinathan<sup>1</sup> and Ram Kesh Yadav<sup>8</sup>

## ABSTRACT

We carried out deep and wide-field near- and mid-infrared observations for a sample of 8 bright-rimmed clouds (BRCs). Supplemented with the *Spitzer* archival data, we have identified and classified 44 to 433 young stellar objects (YSOs) associated with these BRCs. The Class I sources are generally located towards the places with higher extinction and are relatively closer to each other than the Class II sources, confirming that the young protostars are usually found in regions having denser molecular material. On the other hand the comparatively older population, Class II objects, are more randomly found throughout the regions, which can be due to their dynamical evolution. Using the minimal sampling tree analyses, we have extracted 13 stellar cores of 8 or more members, which contains 60% of the total YSOs. The typical core is  $\sim 0.6$  pc in radii and somewhat elongated (aspect ratio of 1.45), of relatively low stellar density (surface density  $60 \text{ pc}^{-2}$ ), consisting of a small (35) number of YSOs of relatively young sources (66% Class I), and partially embedded (median  $A_K = 1.1$  mag). But the cores show a wide range in their mass distribution ( $\sim 20$  to  $2400 M_\odot$ ) with a median value of around  $130 M_\odot$ . We have found the star formation efficiencies in the cores to be between 3% and 30% with an average of  $\sim 14\%$ , which agree with the efficiencies needed to link the core mass function to the initial mass function. We also found a linear relation between the density of the clouds and the number of YSOs. The peaked nearest neighbor spacing distributions of the YSOs and the ratio of Jeans lengths to the YSOs separations indicates a significant degree of non-thermally driven fragmentation in these BRCs.

*Subject headings:* - stars: formation - stars:pre-main-sequence

<sup>1</sup>Aryabhata Research Institute of Observational Sciences (ARIES), Manora Peak, Nainital, 263 001, India, saurabh@aries.res.in

<sup>2</sup>Departamento de Física y Astronomía, Universidad de Valparaíso, Ave. Gran Bretaña 1111, Valparaíso, Chile

<sup>3</sup>Tata Institute of Fundamental Research, Homi Bhabha Road, Colaba, Mumbai - 400 005, India

<sup>4</sup>European Southern Observatory, Karl-Schwarzschild-Str. 2, 85748 Garching bei München, Germany

<sup>5</sup>Kokugakuin University, Higashi, Shibuya-ku, Tokyo 150-8440, Japan

<sup>6</sup>Institute of Astronomy, University of Tokyo, 2-21-1 Osawa, Mitaka, Tokyo 181-0015, Japan

<sup>7</sup>Millennium Institute of Astrophysics, Chile

<sup>8</sup>National Astronomical Research Institute of Thailand, Chiang Mai, Thailand

## 1. Introduction

Observations of embedded star-forming regions (SFRs) show that stellar distributions in SFRs are often elongated, clumpy, or both (see Lada & Lada 2003; Gutermuth, Megeath, Pipher et al. 2005; Gutermuth, Myers, Megeath et al. 2008; Teixeira, Lada, Young et al. 2006; Allen, Megeath, Gutermuth et al. 2007; Koenig, Allen, Gutermuth et al. 2008) and seems to be correlated with the distribution of dense gas of the natal molecular clouds (Gutermuth, Myers, Megeath et al. 2008). Mapping the spatial distribution of young stellar objects (YSOs) within these SFRs is an important means by which one can study the star formation scenario in the region and understand the physical processes that influence star forma-

tion (Koenig, Allen, Gutermuth et al. 2008).

Surveys of molecular clouds in the nearest 1 kpc show that approximately 75% of embedded young stars are in groups and clusters with 10 or more members (Carpenter, Heyer, & Snell 2000; Allen, Megeath, Gutermuth et al. 2007; Zinnecker, McCaughrean, & Wilking 1993). Gutermuth, Megeath, Myers et al. (2009) have isolated several young stellar cores associated with each of a sample of 36 young stellar clusters and have studied their structures. Quantitative statistical properties of these structures, especially the sizes, densities and morphologies of young stellar cores could be used to test the theoretical models of star formation (Kuhn, Feigelson, Getman et al. 2014; Schmeja, Gouliermis, & Klessen 2009). While stars in some SFRs are centrally concentrated with a smooth radial density gradient, in other SFRs stars show signs of fractal sub-clustering. How the different structures are connected to the environmental conditions of the molecular clouds and how they depend on the evolutionary stage of the cluster are not yet clear.

Bright-rimmed clouds (BRCs), which are small, more or less isolated molecular clouds found at the edges of large HII regions, usually show the presence of a group of young stars near the heads of a pillar of gas that point towards the central O/B stars in the region. These clouds may have resulted through the compression of pre-existing molecular clumps in the molecular cloud via a photoionisation-induced shock and are potential sites of triggered SFRs (known as radiatively-driven implosion: RDI; Bertoldi 1989; Lefloch & Lazareff 1994). Numerical simulations on the dynamical evolution of a molecular clump illuminated by the ionizing radiation of OB stars can be very useful for understanding the RDI process (e.g., Miao, White, Nelson et al. 2006).

Relative isolation and simple geometry of BRCs make them an ideal laboratory to observationally test the RDI star formation. Sugitani and collaborators (Sugitani, Fukui, & Ogura 1991; Sugitani & Ogura 1994) compiled a catalog of 89 BRCs (commonly referred to as the SFO catalog) spread throughout the Galaxy; 44 clouds located in the northern hemisphere and 45 clouds located in the southern hemisphere. These clouds were identified by correlating IRAS point sources - having colors consistent with embedded proto-

stars - with clouds displaying optically bright rims from the Sharpless HII region catalog (Sharpless 1959) and the ESO(R) Southern Hemisphere Atlas. Using the submillimetre continuum observations, Morgan, Thompson, Urquhart et al. (2008) have demonstrated the presence of at least one core in 39 of the 45 BRCs studied by them. The morphology of these BRCs is, in general, supportive of the scenario seen in RDI models; a dense core at the head of an elongated column along with the presence of young stars. Urquhart, Morgan, & Thompson (2009) have used CO, mid-infrared (MIR) and radio data to identify 24 of the 45 southern BRCs that are undergoing a strong interaction with their HII region and have classified them as triggered candidates. Fourteen of these 24 interacting BRCs were found to show active star formation on the basis of them being associated with embedded MIR point sources. The remaining BRCs did not show any sign of triggered star formation or they were at an earlier evolutionary stage of star formation. Whilst some individual clouds from the SFO catalog have been studied in detail (e.g. Lefloch, Lazareff, & Castets 1997; Megeath & Wilson 1997; Codella, Bachiller, Nisini et al. 2001; Thompson & White 2004; Urquhart, Thompson, Morgan et al. 2004, 2006, 2007; Urquhart, Morgan, & Thompson 2009; Morgan, Thompson, Urquhart et al. 2008) and have been shown to harbor protostellar cores, the question of whether star formation is a common occurrence within BRCs is still unresolved (Morgan, Thompson, Urquhart et al. 2008). It is essential to carry out a census of YSOs in these SFO BRCs to determine the present status of star formation within them and to relate it to their physical properties and morphologies. In particular, a systematic statistical study of the structure of the resultant stellar systems of BRC star forming activities adjacent to HII regions under the influence of high mass O/B stars has not been made to date.

The main aim of the present study is to investigate statistically the star forming activities in BRCs, especially the structure of the resultant stellar systems or aggregates and its possible origin. Therefore, for our study, we have selected eight triggered BRCs (cf. Table 1) from the SFO catalog which are currently showing active star formation. These BRCs are

located at heliocentric distances ranging from 0.95-2.80 kpc and are distributed in the Galactic longitude ( $l$ ) between 250 and 340 degrees and latitude  $|b| < 3$  degrees. Distances of these BRCs have been taken from the available literature (Urquhart, Morgan, & Thompson 2009; Yamaguchi, Saito, Mizuno et al. 1999, and references therein). These distances were derived mostly from the photometric data of the O type stars which are being assigned as the exciting star(s) of the HII regions in which these BRCs are located. For bright stars at the distance of 1-3 kpc, one can expect small photometric errors ( $< 1 - 2\%$ ), and after taking care of the errors associated with intrinsic main sequence (MS), reddening values and fitting, we can safely assume that the error in the distances can be  $\sim 5-15\%$  (Phelps & Janes 1994).

In the optical, the challenges in studying BRCs are their association with high column density molecular clouds. Wide-field near-infrared (NIR) cameras installed on moderate size telescopes is needed to probe BRCs with sensitivity to detect sub-solar mass objects as well as the angular resolution to resolve high-density groupings or aggregates of stars. The wider field-of-view (FOV) is also necessary to observe the distribution of stars over multiparsec distances (cf. Gutermuth, Megeath, Pipher et al. 2005). In the present study, we carry out deep NIR observations with Infrared Side Port Imager (ISPI) camera on the 4m Blanco telescope at Cerro Tololo Inter-American Observatory (CTIO). We also utilized the infra-red (IR) data from the *Spitzer* archive around these BRCs (except SFO 79, which has no *Spitzer* data) to identify deeply embedded YSOs associated with them. The spatial distribution of these YSOs has been compared to that of the surroundings as a function of their evolutionary status. According to the simulations shown by Miao, White, Nelson et al. (2006), the cloud cores of BRCs have sizes between 1-2 pc. The range of the distances of the selected BRCs are  $\sim 1-3$  kpc, therefore, the  $10 \times 10$  arcmin square FOV of ISPI camera will correspond to 3-9 pc, which is sufficient to cover the BRC regions necessary for our analyses. We are using new quantitative techniques for analyzing the spatial structures of the aggregates to reveal the presence of compact cores and to compare the properties of these cores

with those found in other SFRs. These YSO cores' properties (density, size, etc.) have been used to infer the history of star formation in the parental molecular cloud.

In this paper, Section 2 describes the observations and data reduction. The YSO identification technique, the completeness of the resultant YSOs sample, and their spatial distribution, mainly with respect to the associated molecular clouds, is discussed in Section 3. The methods for finding the aggregate cores and the active regions are also explained in Section 3. In Section 4, we will discuss our results and will conclude in Section 5.

## 2. Observations and data reduction

Deep NIR broad band observations of the fields containing BRCs along with the *Spitzer* archival data have been used in the present study.

### 2.1. Blanco Observations

NIR ( $J, H, K'$ ) data for eight selected BRCs along with two nearby field regions (cf. Table 1) were collected with the ISPI camera (FOV  $\sim 10.5 \times 10.5$  arcmin<sup>2</sup>; scale 0.3 arcsec/pixel; van der Blik, Norman, Blum et al. 2004) on the 4 m Blanco telescope at CTIO, Chile during the nights of 2010 March 03 to 04. The seeing was  $\sim 1$  arcsec. The individual exposure times were 60 s per frame for all the filters. We used a set of  $3 \times 3$  grid pattern, with 1 arcmin step, to compensate for the cosmetic effects of the detectors, and to create a sky image for the sky subtraction. The total exposure time for the target fields were 540 s for each  $J, H$  and  $K'$  bands. Dome flats and dark frames were taken at the beginning and end of each night. Data reduction followed the usual steps for NIR data: dark subtraction, flat-fielding, sky subtraction, alignment and averaging of sky-subtracted frames for each filter separately. The dome flats were also used to flag bad pixels. The sky frames were median combined and subtracted from the science images. In Fig. 1, we have shown the color composite image of the SFO 54 region made by using the clean  $J, H$  and  $K'$  band images of  $10.5 \times 10.5$  arcmin<sup>2</sup> field.

The PSF-fitting stellar photometry on these sky-subtracted and combined images was carried out by using the *find, phot, psf* and *allstar* routines within DAOPHOT (Stetson 1994). The cali-

bration of the photometry to the standard system was done by using the transformation equations:

$$(J - K) = M1 \times (j - k) + C1 \quad (1)$$

$$(H - K) = M2 \times (h - k) + C2 \quad (2)$$

$$(K - k) = M3 \times (H - K) + C3 \quad (3)$$

where the capital  $JHK$  are the standard magnitudes of the common stars taken from the Two Micron All Sky Survey (2MASS) catalog which provides absolute photometry in the  $J$  ( $1.25 \mu\text{m}$ ),  $H$  ( $1.65 \mu\text{m}$ ), and  $K_s$  ( $2.17 \mu\text{m}$ ) bands down to a limiting magnitude of 15.8, 15.1, and 14.3, respectively, with a signal-to-noise ratio greater than 10. The small  $jhk$  and Ms & Cs are the instrumental ISPI magnitudes and the transformation coefficients, respectively. In Fig. 2, as an example of the fit for the transformation coefficients of the ISPI data to the 2MASS data is shown for the sources in the SFO 54 region. The values of these coefficients are given in Table 2 along with the standard errors ( $\sim 0.01$ - $0.02$  for the zero point (C) and less than  $0.03$  for the color term (M)). The typical DAOPHOT errors in magnitude as a function of corresponding magnitudes are shown in Fig. 3. It can be seen that the errors become large ( $0.2$  mag) for stars fainter than  $K = 18.5$  mag, so the measurements beyond these magnitudes are not reliable and were not used in this study.

Because of the higher number of detected stars in  $K$  and  $H$  bands, we have used the  $H - K$  color to calibrate  $K$  magnitude. Therefore, in the final catalog, we have only those stars which are detected in at least  $K$  and  $H$  bands and found by merging the individual photometric catalog by a search radius of  $0.3$  arcsec. We have done the alignment of the individual frames using the IMALIGN task of IRAF<sup>1</sup> with an accuracy better than  $0.1$  arcsec; our  $0.3$  arcsec match threshold should match sources for upto  $3\sigma$  positional errors. In a few cases when there was a second astrometric match, we adopted the closer match for our final

merged catalog. We used the  $K$  band position for astrometry of the final catalog. Stars brighter than  $10$  mag in  $K$  are saturated in our observations, so we have taken their respective magnitude from the 2MASS point source catalog. The final catalog contains  $2000$ - $15000$  sources per field depending on the crowding/nebulosity in the region.

## 2.2. *Spitzer* observations

We have used the archived data taken from the Infrared Array Camera (IRAC; Fazio, Hora, Allen et al. 2004) of the space-based *Spitzer* telescope at  $3.6 \mu\text{m}$ ,  $4.5 \mu\text{m}$ ,  $5.8 \mu\text{m}$  and  $8.0 \mu\text{m}$  bands. We obtained basic calibrated data (BCD) from the *Spitzer* data archive for all the BRCs, except for SFO 76. The exposure time of each BCD was  $10.4$  sec and for creating a mosaic, few hundreds of BCDs have been used. Mosaicing in each wavelength was performed by the MOPEX software provided by *Spitzer* Science Center (SSC). All of our mosaics were built at the native instrument resolution of  $1.2$  arcsec pixel<sup>-1</sup> with the standard BCDs. All the mosaics were then aligned and trimmed to make a  $10.5 \times 10.5$  arcmin<sup>2</sup> box size containing the same area as observed in the ISPI observations. These trimmed sections have been used for further analyses. Some of the studied regions were not fully observed in the outer parts ( $<10\%$  of the whole area) in all the four channels of IRAC but it does not affect our analyses, since our region of interest is always closer to the image center containing the H II regions.

We used the *DAOPHOT* package in IRAF to detect sources and to perform photometry in each of the IRAC mosaics. The FWHM of every detection was measured and all detections with a FWHM  $>3.6$  arcsec were considered resolved and were removed. The detections were also examined visually in each band to remove non-stellar objects and false detections. In order to avoid source confusion due to crowding, *PSF* photometry for all the sources was carried out. Aperture photometry for well isolated sources was first done by using an aperture radius of  $3.6$  arcsec with a concentric sky annulus of the inner and outer radii of  $3.6$  and  $8.4$  arcsec, respectively. The FWHM of the star's intensity profile were between  $2.4$  -  $3.6$  arcsec in different IRAC bands. As the studied regions are nebulous and sometimes crowded, the inner bright region of the intensity profile ( $\sim 1 \times$

<sup>1</sup>IRAF is distributed by the National Optical Astronomy Observatory, which is operated by the Association of Universities for Research in Astronomy (AURA) under a cooperative agreement with the National Science Foundation.

FWHM: 3.6 arcsec) of stars has been used to derive the aperture magnitude. This will lose some photons from the outer wings of the intensity profile of stars. Since this profile behaves like a Gaussian, at  $3 \times \text{FWHM}$  radii, around  $\sim 99\%$  of star photons can be considered integrated. Therefore, we have applied the aperture correction as a difference in aperture magnitudes at these two radii, as has been suggested in the IRAC Handbook for data reduction<sup>2</sup>. We adopted the zero-point magnitudes, for the standard aperture radius of 12 arcsec ( $\sim 3 \times \text{FWHM}$ ) and background annulus of 12-22.4 arcsec, as 19.670, 18.921, 16.855 and 17.394 in the 3.6  $\mu\text{m}$ , 4.5  $\mu\text{m}$ , 5.8  $\mu\text{m}$  and 8.0  $\mu\text{m}$  bands, respectively (IRAC data Handbook). The necessary aperture corrections for the *PSF* photometry were also calculated as a difference between aperture and *PSF* magnitudes of the selected well-isolated sources and were applied to the *PSF* magnitudes of all the sources.

The sources with photometric uncertainties  $< 0.2$  mag in each band were considered as good detections and are used in further analyses. Around 600-1900 sources have been detected in 3.6  $\mu\text{m}$  in different regions with fewer detections at longer wavelengths. This may be because the shorter wavelength channels are more sensitive and less affected by the bright diffuse emission that dominates the 5.0  $\mu\text{m}$  and 8.0  $\mu\text{m}$  observations. The underlying typical stellar photosphere is also intrinsically fainter at 5.0  $\mu\text{m}$  and 8.0  $\mu\text{m}$  than at 3.6  $\mu\text{m}$  and 4.5  $\mu\text{m}$ . The typical magnitude limits of the data in the 3.6  $\mu\text{m}$ , 4.5  $\mu\text{m}$ , 5.8  $\mu\text{m}$  and 8.0  $\mu\text{m}$  bands having  $S/N > 5$  (error  $\leq 0.2$  mag) were found to be  $\sim 16.0$ , 15.5, 13.0 and 12.8 mag, respectively, but they varied from region to region. The NIR ISPI counterparts of the IRAC sources were then searched for within a radius of 1 arcsec.

### 3. Results

#### 3.1. Strategy of YSO identification

The YSOs are usually grouped in an evolutionary sequence representing: accreting protostars (Class 0), evolved protostars (Class I), classical T-Tauri stars (CTTSs: Class II) and weak-line T-Tauri stars (WTTSs: Class III) (cf.

Feigelson & Montmerle 1999). The YSOs of earlier stages are usually deeply buried inside the molecular clouds hence it is difficult to detect them at optical wavelengths. The most prominent feature of these YSOs is the accreting circumstellar disks. The radiations from the central YSO are more or less absorbed by these circumstellar material and re-emitted in IR. Therefore, excepting Class III sources these YSOs with disks can be probed through their IR excess (compared to normal stellar photospheres).

However, observations of YSOs in SFRs such as Taurus Auriga show a wide dispersion ( $\sim 1$ -10 Myr) in the lifetimes of circumstellar disks (Strom, Strom, Edwards et al. 1989; Haisch, Lada, & Lada 2001; Armitage, Clarke, & Palla 2003). Recently, Kraus, Ireland, Hillenbrand et al. (2012) studied excess emission in Taurus binaries over NIR to millimeter wavelengths and concluded that the prompt disk dispersal only occurs for a small fraction of single stars, and that  $\sim 80\% - 90\%$  retains their disks for at least  $\sim 2$ -3 Myr (but rarely for more than  $\sim 5$  Myr). The YSO census based on IR excesses is not complete since it detects only YSOs having an accreting disk. But we are interested in whether our target BRCs have been showing star forming activities in the last couple of Myr, this limitation is small where few YSOs have had sufficient time for their disks to disperse (cf. Hernández, Hartmann, Calvet et al. 2008; Haisch, Lada, & Lada 2001; Gutermuth, Megeath, Myers et al. 2009; Gutermuth, Pipher, Megeath et al. 2011).

The ISPI data along with the *Spitzer* IRAC data have been used to identify and classify the YSOs associated with the BRCs based on their excess emission in IR by using the following classification schemes.

##### 3.1.1. Step 1: IRAC four-band YSO classification scheme:

We have applied Step 1 to all sources which are detected in all four IRAC bands. We separated out IR excess contaminants such as star forming galaxies, broad-line active galactic nuclei, unresolved shock emission knots, objects that suffer from polycyclic aromatic hydrocarbon (PAH) emissions etc., by applying constraints in various color spaces (Gutermuth, Megeath, Myers et al. 2009).

<sup>2</sup>[http://irsa.ipac.caltech.edu/data/SPITZER/docsirac/iracinstrumenthandbook/IRAC\\_Instrument\\_Handbook.pdf](http://irsa.ipac.caltech.edu/data/SPITZER/docsirac/iracinstrumenthandbook/IRAC_Instrument_Handbook.pdf)

To minimize the inclusion of faint extra-galactic contaminants, a brightness limit to IRAC magnitudes has been applied. Also to discriminate out brighter contaminants, various IRAC color spaces along with magnitude limits have been used. Active star forming galaxies have a very strong PAH features yielding very red 5.8 and 8.0  $\mu\text{m}$  colors (the 6.2  $\mu\text{m}$  and 7.7  $\mu\text{m}$  PAH features are much stronger than the 3.3  $\mu\text{m}$  PAH feature: Stern, Eisenhardt, Gorjian et al. 2005), which can therefore be very well separated out from YSOs by using IRAC two-color diagrams (TCDs). The resultant sample will have negligible residual contaminants (Gutermuth, Megeath, Myers et al. 2009). Broad line AGN having MIR colors consistent with YSOs (Stern, Eisenhardt, Gorjian et al. 2005) can also be separated out from YSOs simply by applying IRAC color selections. In  $[5.8 - 8.0]$  vs.  $[3.6 - 4.5]$  TCD, the broad line AGNs lie along a vertical branch because of the lack of strong PAH feature at 5.8  $\mu\text{m}$  and 8.0  $\mu\text{m}$  and dominating power law emission peaking at 1.6  $\mu\text{m}$  (Stern, Eisenhardt, Gorjian et al. 2005). Color/magnitude selection criteria based on Gutermuth, Megeath, Myers et al. (2009) has been used to eliminate these AGNs. Even after applying these cut-offs, we can still expect  $\sim 8$  contaminants per square degree (Gutermuth, Megeath, Myers et al. 2009). But our FOV is  $\sim 10 \times 10$  arcmin square, therefore the resultant contaminants will be very low ( $\sim 0.2$  contaminant per field).

We, then isolated YSOs with IR excess from those without IR excess and classified them as Class I or as Class II YSOs based on their prominence at longer wavelengths. In Fig. 4, we have shown the  $[3.6 - 5.8]$  vs  $[4.5 - 8.0]$  TCD for all the IRAC sources in all regions studied, where Class I and Class II sources are represented by green star and green open square symbols, respectively. The identified contaminating sources are shown by blue dots.

### 3.1.2. Step 2: $K$ , $[3.6]$ , $[4.5]$ three band YSO classification scheme:

Since the studied regions are highly nebulous, the YSO selection based on the IRAC four band photometry may not be complete as many sources falling in these regions could not be detected at longer wavelengths due to the saturation of detectors. Therefore, we apply Step 2 to those

sources that lack detection at either 5.8  $\mu\text{m}$  or 8.0  $\mu\text{m}$ , but have NIR detection in the ISPI  $K$  band. In Fig. 4, we have plotted de-reddened  $[3.6 - 4.5]_0$  vs  $[K - 3.6]_0$  TCD for the sources detected in  $K$ , 3.6  $\mu\text{m}$  and 4.5  $\mu\text{m}$  bands in all regions studied. The following procedure outlined in Gutermuth, Megeath, Myers et al. (2009) has been used to classify sources as Class I (blue stars) and as Class II (blue squares) YSOs. To estimate the reddening, we have used the NIR TCD (cf. §3.1.4). Stars having  $[J - H]$  color  $\geq 0.6$  mag and lying above the CTTS locus or its extension are traced back to CTTS locus or its extension to get their intrinsic colors. The difference between the intrinsic color and the observed one would give the extinction value. Once we have the extinction value for the individual stars, we generated an extinction map for the whole BRC region. The extinction values in the sky plane were calculated with a resolution of 5 arcsec by taking the mean of extinction value of stars in a box having a size of 17 arcsec, and then were used to deredden the remaining stars. In the above procedure, we have assumed the normal extinction law ( $R_V = 3.1$ ) to back-trace the stars to the CTTS locus. In many SFRs,  $R_V$  tends to deviate from normal, preferably towards the higher values, for example:  $R_V = 3.7$  (Kumar, Sharma, Manfroid et al. 2014, Carina region),  $R_V = 3.3$  (Pandey, Eswaraiah, Sharma et al. 2013, NGC 1931),  $R_V = 3.5$  (Sharma, Pandey, Pandey et al. 2012, NGC 281) and  $R_V = 3.7$  (Pandey, Sharma, Ogura et al. 2008, Be 59). But the difference between  $R_V = 3.1$  and  $R_V = 3.7$  would make only a small effect in near and mid IR region, since for  $\lambda > \lambda_I$ , the reddening law can be taken as a universal quantity (Cardelli, Clayton, & Mathis 1989; He, Whittet, Kilkenny et al. 1995).

### 3.1.3. Step 3: $H$ , $K$ two-band YSO classification scheme:

We applied Step 3 to all the detections in the ISPI  $H$  and  $K$  bands. The scheme, explained in detail by Kumar, Sharma, Manfroid et al. (2014), compares the dereddened color-magnitude diagrams (CMDs) of equal area of the studied region and nearby field region (cf. §2.1). The dereddened magnitudes and colors were obtained by using the extinction map as discussed in the previous section. In Fig. 5, as an example, we have plotted

the de-reddened NIR CMDs,  $K_0$  vs  $(H - K)_0$ , for both SFO 55 and the nearby field region. The blue dashed curve is the outer envelop of the field stars and the thick red curve is the same curve reddened by  $A_V = 5$  mag to make allowance for the scattering due to the clumpy nature of the molecular clouds (Kumar, Sharma, Manfroid et al. 2014). A comparison of the CMDs reveals many sources of  $(H - K)_0 \gtrsim 0.6$  mag in the BRC region, suggesting significant IR excesses in the  $K$  band. All the stars having a color ‘ $(H - K)_0 - \sigma_{(H - K)_0}$ ’ larger than the RED cut-off curve (shown as a red solid curve in Fig. 5, see for detail Kumar, Sharma, Manfroid et al. 2014) might have an excess emission in the  $K$  band and thus can be considered as probable YSOs (see also Ojha, Tamura, Nakajima et al. 2004a; Mallick, Ojha, Samal et al. 2012). While these stars are probably dominated by YSOs, still they could be contaminated by variable stars, dusty asymptotic giant branch stars, unresolved planetary nebulae and background galaxies (Robitaille, Meade, Babler et al. 2008; Povich, Smith, Majewski et al. 2011). However, since there are no stars located in the field CMD redward of the RED envelope and neither of these IR excess sources fall on similar positions of previously identified contaminants (cf. §3.1.1), we assume they are most probably YSOs with IR excess.

### 3.1.4. Step 4: $J, H, K$ three-band YSO classification scheme:

The sources detected in all three ISPI bands ( $JHK$ ) have been used to further classify YSOs according to their evolutionary stages by using the conventional NIR TCD. In Fig. 6, we have plotted the NIR TCD for the stars in all the regions studied. All the ISPI magnitudes and colors have been converted into the California Institute of Technology (CIT) system<sup>3</sup>. The solid and thick dashed curves represent the un-reddened MS and giant branch (Bessell & Brett 1988), respectively. The dotted line indicates the locus of un-reddened CTTSs (Meyer, Calvet, & Hillenbrand 1997). All the curves and lines are also in the CIT system. The parallel dashed lines are the reddening vectors drawn from the tip (spectral type M4) of the giant branch (“upper reddening line”), from the base (spectral type A0) of the MS branch

(“middle reddening line”) and from the tip of the intrinsic CTTS line (“lower reddening line”). The extinction ratios  $A_J/A_V = 0.265$ ,  $A_H/A_V = 0.155$  and  $A_K/A_V = 0.090$  have been taken from Cohen, Persson, Elias et al. (1981). We classified the sources according to three regions in this diagram (cf. Ojha, Tamura, Nakajima et al. 2004b). The ‘F’ sources are located between the upper and middle reddening lines and are considered to be either field stars (MS stars, giants) or Class III and Class II sources with small NIR excess. ‘T’ sources are located between the middle and lower reddening lines. These sources are considered to be mostly CTTSs (or Class II objects) with large NIR excess. There may be an overlap of Herbig Ae/Be stars in the ‘T’ region (Hillenbrand, Strom, Vrba et al. 1992). ‘P’ sources are those located in the region redward of the lower reddening line and are most likely Class I objects (protostellar-like objects: Ojha, Tamura, Nakajima et al. 2004b). It is worth while to mention also that Robitaille, Whitney, Indebetouw et al. (2006) have shown that there is a significant overlap between protostars and CTTSs. All sources have been designated as CTTSs if they satisfy the criteria that they fall in the ‘T’ region of the NIR TCD (Fig. 6) and lie redward of the blue dotted cut-off line of the de-reddened CMD (cf. Fig. 5). They are shown as open triangles in Fig. 6. We have also plotted the previously identified probable IR excess sources (open circles) having  $J$  band detection. Most of these sources are located in the ‘P’ region in Fig. 6, which means that they are most likely Class I objects.

## 3.2. The YSO sample and its completeness

We have thus identified and classified 44 to 433 YSOs in our BRCs based on their excess emission in IR. In total 1347 YSOs have been identified, out of which 790 are Class I protostars. We have made a catalog of the YSOs for each BRC identified in the present study. In Table 3, we have given a sample of these YSOs along with their positions, magnitudes at various bands and the flags for the scheme used to classify them. A complete table is available in electronic form only.

To understand the level of star formation at present or in the past in our BRCs, it is important to know the completeness limits in terms of masses for the sample of YSOs identified in each

<sup>3</sup><http://www.astro.caltech.edu/~jmc/2mass/v3/transformations/>

region. The photometric data may be incomplete due to various reasons, e.g., background nebulosity, crowding of stars, the detection limit etc. For the current sample, the YSOs are identified either, if they are detected in at-least two *Spitzer* IRAC channels (3.6  $\mu\text{m}$  and 4.5  $\mu\text{m}$ , Steps 1 and 2), or if they are detected in two ISPI *H* and *K* bands (Steps 3 and 4). In Fig. 7 (top left panel), we have plotted IRAC 3.6  $\mu\text{m}$  mag vs. ISPI *K* mag for the sources detected in the SFO 54 region. From the figure, it is clear that the faintest source in 3.6  $\mu\text{m}$  band ( $\sim 16.5$  mag) corresponds to those of *K*  $\sim 15.5$  mag. The *K* band has yielded much fainter detections ( $\sim 18.5$  mag), therefore the completeness of our photometric data taken from ISPI will dictate the completeness of the current sample of YSOs.

To determine the completeness factor (CF) for ISPI data, we used the ADDSTAR routine of DAOPHOT II. This method has been used by various authors (see Sharma, Pandey, Ojha et al. 2007; Sharma, Pandey, Ogura et al. 2008, and references therein). Briefly, the method consists of randomly adding artificial stars of known magnitudes and positions into the original frame. The frames are reduced by using the same procedure used for the original frame. The ratio of the number of stars recovered to those added in each magnitude interval gives the CF as a function of magnitude. The luminosity distribution of artificial stars is chosen in such a way that more stars are inserted into the fainter magnitude bins. In all about 15% of the total stars are added so that the crowding characteristics of the original frame do not change significantly (see Sagar & Richtler 1991). As an example, the CF for the SFO 54 region (distance = 0.95 kpc) is given in the top right panel of Fig. 7 for different ISPI bands. In the same panel, we have also plotted the *K* band CFs for a nearby field region (shown by grey dotted curve ' $K_F$ ') as well as for the SFO 64 region (distance = 2.7 kpc, shown by black solid curve ' $K_C$ '), representing a field free from nebulosity and that of higher crowding, respectively. Higher crowding, in the case of SFO 64 can be attributed to its intrinsic property or its farther distance. The field region has the highest completeness because of the lack of nebular backgrounds. Out of SFO 64 and SFO 54, both having a similar level of nebulosity, SFO 64 shows a lower CF because of its larger

distance and/or higher crowding.

In the lower panel of Fig. 7, we have plotted the (*H* - *K*) vs *K* CMD for the SFO 54 region along with the theoretical MS isochrone of 2 Myr ( $Z = 0.02$ ) by Marigo, Girardi, Bressan et al. (2008) and the pre-main sequence (PMS) isochrones of age 1 and 5 Myr by (Siess, Dufour, & Forestini (2000) (for mass  $> 1.2 M_\odot$ ) and Baraffe, Chabrier, Allard et al. (1998) (for mass  $< 1.2 M_\odot$ ), all corrected for the distance (cf. Urquhart, Morgan, & Thompson 2009) and the foreground expected reddening ( $A_{K_{foreground}} = 0.15 \times D$ , where  $D$  is the distance in kpc, Indebetouw, Mathis, Babler et al. 2005). The slanting parallel dashed lines represent the reddening vectors for PMS stars of different masses. The dotted and solid broken lines represent the 90% and 50% completeness limits for the data as inferred from the CF calculated earlier. We have taken into account the effect of color (*H* - *K*) on the completeness limit of this CMD. We can easily see that the 90% and 50% completeness limits correspond to  $\sim 0.04 M_\odot$  and  $\sim 0.03 M_\odot$  YSOs, respectively. However, the photometric errors at this level should be higher ( $\pm 0.1$  mag to  $\pm 0.2$  mag), therefore, the corresponding errors in the derived mass should be of the order of  $\sim \pm 0.02 M_\odot$  to  $\pm 0.03 M_\odot$ . The 90% and 50% completeness limits for the YSOs embedded deeply in the molecular cloud (corresponding to the peak  $A_K$  value taken from Table 5) are considered to be  $\sim 0.15 \pm 0.03 M_\odot$  and  $\sim 0.08 \pm 0.04 M_\odot$ , respectively. In the last column of Table 1, we have given the 90% completeness limit for YSOs corrected for the foreground and peak (including the foreground) reddening for all the studied regions.

The PMS isochrones were used to derive the CF for the sample of YSOs in terms of mass. The errors in the mass of YSOs quoted above comes mainly from the large photometric errors at faint levels. In the *H* - *K* vs. *K* diagram (Fig. 7 lower panel), the PMS isochrones are almost vertical; therefore any change of age in the lower mass regime would shift the isochrones in the vertical direction (magnitude axis), and typically it would cause to  $0.02 M_\odot$  difference for the age difference of 4 Myr (cf. Fig. 7. Lower Panel). From Fig. 6 and Fig. 7 and its siblings for the rest of our BRCs we find that all of them are regions of recent star formation harboring YSOs of various evolutionary



stages from Class 1 (protostars) to at-least Class II (CTTSs), leading to the lower error values in mass determination of YSOs due to their comparatively smaller age spreads.

### 3.3. Distribution of molecular cloud around the BRCs

To study the relationship between the distribution of YSOs and the molecular clumps in the regions, we have derived  $A_K$  extinction maps using the  $(H - K)$  colors of the MS stars (cf. Gutermuth, Pipher, Megeath et al. 2011). This map has also been used to quantify the amount of extinction within each sub-regions of the studied BRCs and to characterize the structures of the molecular clouds within each sub-regions (Jose, Pandey, Samal et al. 2013; Gutermuth, Pipher, Megeath et al. 2011; Gutermuth, Megeath, Myers et al. 2009). The sources showing excess emission in IR can lead to overestimation of extinction values in the derived maps. The excess emission can be of the order of  $\sim 0.25$  mag in  $H - K$  color (Sharma, Pandey, Pandey et al. 2012; Pandey, Sharma, Ogura et al. 2008; Chauhan, Pandey, Ogura et al. 2011) which will correspond to the overestimation of  $A_K$  value by  $\sim 0.4$  mag. This will increase cloud mass estimate which we are going to derive later (§4.2.7). Therefore, to improve the quality of the extinction maps, the candidate YSOs and probable contaminating sources (cf. §3.1) must be excluded from the stars used. In order to determine the mean value of  $A_K$  we used the nearest neighbor (NN) method as described in detail in Gutermuth, Megeath, Pipher et al. (2005) and Gutermuth, Megeath, Myers et al. (2009) to determine the mean value of  $A_K$ . Briefly, at each position in a uniform grid of 5 arcsec, we calculated the mean value of  $(H - K)$  colors of five nearest stars. The sources deviating above  $3\sigma$  were excluded to calculate the final mean color of each point. To convert  $(H - K)$  color excesses into  $A_K$  we used the relation  $A_K = 1.82 \times ((H - K)_{obs} - (H - K)_{int})$ . This is derived from the reddening law by Flaherty, Pipher, Megeath et al. (2007). We have assumed  $(H - K)_{int} = 0.2$  mag as an average intrinsic color for all stars in young clusters (see. Allen, Pipher, Gutermuth et al. 2008; Gutermuth, Megeath, Myers et al. 2009). Of course, the intrinsic color depends on the spectral type, i.e., mass of the MS stars, so, this assump-

tion introduces errors in reddening estimation. But this effect will be small as can be seen in Fig. 7 (bottom panel). The MS for stars for all mass/spectral range is almost vertical. The standard deviation in their  $H - K$  color is of the order of 0.1 mag, which corresponds to the error of  $\sim 0.1 A_K$  in the extinction map. To eliminate the foreground contribution in the extinction measurement, we used only those stars with  $A_K > 0.15 \times D$ , where D is the distance in kpc (Indebetouw, Mathis, Babler et al. 2005) to generate the extinction map. The extinction maps smoothed to a resolution of 5 arcsec and reaching down upto  $A_K \sim 2.8$  mag were generated for all the regions studied. However, the derived  $A_K$  values are to be considered as a lower limits, because the sources with higher extinction may not be detected in our study. As an example, we have shown in Fig. 8 (Left Panel) the derived extinction map for the SFO 54 region.

### 3.4. Spatial distribution of YSOs in the region

By analyzing the stellar density distribution morphology in relation to the molecular cloud structure, observational analyses can address the link between star formation, gas expulsion, and the dynamics of the clusters as well as how these processes guide the evolution of young clusters (Gutermuth, Megeath, Pipher et al. 2005). To study the density distribution of YSOs in the region we have generated their surface density maps using the NN method as described by Gutermuth, Megeath, Pipher et al. (2005). We have taken the radial distance necessary to encompass the 5th nearest YSOs and computed the local surface density (cf. Fig. 8, Right Panel) in a grid size of 5 arcsec. To facilitate comparisons between the stellar density and the gas column density, we adopted the grids identical to the grid size of the extinction map for each region.

The spatial distribution of YSOs in a region can also be analyzed by deriving the typical spacing between them and comparing this spacing to the Jeans fragmentation scale for a self-gravitating medium with thermal pressure (Gomez, Hartmann, Kenyon et al. 1993). We measure the projected distance from each YSO to its nearest YSO neighbor (NN2), as well as to its fifth nearest YSO neighbor (NN6; the radial

distance from each source such that a circular area of that radius centered on the source contains the nearest five neighbors, i.e. a total of six YSOs), and plotted their histograms with a bin size of 0.02 pc in Fig. 9 for all the studied BRCs. All the histograms show a major peak in their distribution along with a couple of smaller peaks indicating groupings/sub-groupings in the regions.

### 3.5. Extraction of YSO's cores embedded in the molecular cloud

All the studied BRCs contain a number of sub-groups/cores of YSOs (cf. Figs. 10 - 17, top left panels) presumably due to fragmentation of the molecular cloud. Physical parameters of these cores, which might have formed in a single star-forming event, play a very important role in the study of star formation. Gutermuth, Megeath, Myers et al. (2009) have applied an empirical method based on the minimal sampling tree (MST) technique to a sample of 36 young stellar clusters to isolate groupings (cores) from the more diffuse distribution of YSOs in nebulous regions. This method effectively isolates the sub-structures without any type of smoothing (e.g., Cartwright & Whitworth 2004; Schmeja & Klessen 2006; Bastian, Ercolano, Gieles et al. 2007; Bastian, Gieles, Ercolano et al. 2009; Gutermuth, Megeath, Myers et al. 2009). The sub-groups detected in this way have no bias regarding the shapes of the distribution and preserve the underlying geometry of the distribution (Gutermuth, Megeath, Myers et al. 2009). In Figs. 10 - 17 (bottom left panels), we have plotted the derived MSTs for the YSOs in the BRC regions studied. The different color dots and lines are the positions of the YSOs and the MST branches, respectively. A close inspection of these figures reveals that all the regions exhibit in-homogeneous structures and there is one major and several other concentrations of YSOs distributed throughout the regions.

In order to isolate the sub-structures, we have to adopt a surface density threshold expressed by a critical branch length. In Fig. 18, we have plotted histograms between MST branch lengths and MST branch numbers for the YSOs. From this plot, it is clear that they have a peak at small spacings and a relatively long tail towards large spacings. These peaked distance distributions typically suggest a significant

sub-region (or sub-regions) above a relatively uniform, elevated surface density. By adopting an MST length threshold, we can isolate those sources which are closer than this threshold, yielding populations of sources that make up local surface density enhancements. To obtain a proper threshold distance, we have used the similar approach as already demonstrated by Gutermuth, Megeath, Myers et al. (2009). In Fig. 18, we have also plotted the cumulative distribution function (CDF) for the branch length of YSOs for MST. In this distribution, we can see three line segments: a steep-sloped segment at short spacings, a transition segment that approximates curved character of the intermediate length spacings, and a shallow-sloped segment at long spacings (cf. Gutermuth, Megeath, Myers et al. 2009). Typically, most of the sources are found in the steep segment, where the spacings are small, e.g., in a core of the stellar distribution. Therefore, to isolate the core region in the BRCs, we have fitted by two true lines in shallow and steep segment of the CDF and extended them to connect together. We adopted the intersection point between these two lines as the MST critical branch length, as shown in Fig. 18 (see also, Gutermuth, Megeath, Myers et al. 2009). The BRC cores were then isolated from the lower density distribution by clipping MST branches longer than the critical length found above. Similarly, we have enclosed all the YSOs associated with the BRC by selecting the point where the curved transition segment meets the shallow-sloped segment at longer spacings. We have called this region in the BRC as its active region where recent star formation took place or contains YSOs moved out from the cores due to dynamical evolution. Black dots and black MST connections in Figs. 10 - 17 (bottom left panels) represent the more closely spaced YSOs than the critical length. In this way we can very easily pick up the major groupings of the YSOs along with some other sub-groupings scattered in the regions. We have then plotted the respective convex hull (cf. Gutermuth, Megeath, Myers et al. 2009) for these cores and for the whole active SFR region in Figs. 10 - 17, lower panels (solid red and solid grey lines, respectively). The physical details of these sub-groups (cores) and the active regions are given in Tables 4 - 6. The median value of the critical

branch lengths for the cores and the active regions are 0.18 pc and 0.30 pc, respectively.

## 4. Discussion

### 4.1. General trends in the spatial distributions

In this Section, we investigate the distribution of the YSOs, their separation, and their relation to the associated molecular clouds as a function of their evolutionary status.

#### 4.1.1. YSOs and their association with the surrounding molecular cloud

The identification of YSOs (cf. §3) in a sample of eight BRCs which are classified as triggered by Urquhart, Morgan, & Thompson (2009) reveals recent star formation in them. A newer observational characterization of the relationship between the spatial distribution of the YSOs and their associated cloud material is vital to understand the nature of their spatial distribution, to constrain the model of star formation, and to ascertain the underlying physics (e.g., Bate & Bonnell 2005; Krumholz & Tan 2007; Myers 2009; Gutermuth, Pipher, Megeath et al. 2011). We have studied the spatial distribution of the YSOs in and around the BRCs by superimposing them on the  $\sim 10' \times 10'$  color-composite image obtained from the 8.0  $\mu\text{m}$  (red); 3.6  $\mu\text{m}$  (green) and  $K$  (blue) band images (Figs. 10 - 17 (top left panels)). The yellow and red dots are Class I and Class II objects, respectively. The distribution of gas and dust as seen by the MIR emissions along with the several concentrations of YSOs can be easily seen in the images. The distribution of YSOs reveals that a majority of Class I sources belong generally to these concentrations, whereas the comparatively older population, i.e. Class II objects, are rather randomly distributed throughout the region.

Star formation usually takes place inside the dense cores of molecular clouds and the YSOs often follow clumpy structures of their parental molecular clouds (see e.g. Gomez, Hartmann, Kenyon et al. 1993; Lada, Alves, & Lada 1996; Motte, Andre, & Neri 1998; Allen, Myers, Di Francesco et al. 2002; Gutermuth, Megeath, Pipher et al. 2005; Gutermuth, Myers, Megeath et al. 2008; Teixeira, Lada, Young et al. 2006; Winston, Megeath, Wolk et al. 2007). The IR extinction maps can be used

to represent the column density distribution of the molecular cloud associated with BRCs (cf. Gutermuth, Megeath, Myers et al. 2009; Jose, Pandey, Samal et al. 2013). We have compared the isodensity contours of YSOs with the extinction maps (Figs. 10 - 17; top right panels), and found that most of the YSOs are distributed in groups in the regions of detectable extinction. Gutermuth, Pipher, Megeath et al. (2011) also found similar trends in eight nearby molecular clouds. They have reported a power-law correlation between the local surface densities of YSOs and the column density of gas (as traced by NIR extinction), agreeing with the prediction of the thermal fragmentation of a sheet-like isothermal layer. If we compare the extinction contours with the IRAC 8.0  $\mu\text{m}$  images (Figs. 10 - 17 (top left panels)), they roughly follow each other's distribution except in one or two BRCs, but the peaks do not match well. IRAC 8.0  $\mu\text{m}$  band includes the PAH emission and its intensity would be the strongest in the photo-dissociation region (PDR) which faces the ionizing source. The extinction contours, on the other hand, would indicate the distribution of the molecular cloud. Therefore, there may be instances where the IRAC and extinction maps don't match well. Also, the cut-off in the 8.0  $\mu\text{m}$  intensity and extinction contours can raise some differences in these two distributions.

Schmeja, Kumar, & Ferreira (2008) studied the spatial distribution of different classes of YSOs in embedded clusters and found that they mostly evolve from a hierarchical to a more centrally concentrated distribution. Gutermuth, Myers, Megeath et al. (2008) have shown that the sources in each of the Class I and Class II evolutionary states have very different spatial distributions relative to the distribution of the dense gas in their natal cloud. We have also compared the extinction maps with the positions of YSOs of different evolutionary status and found that the Class I sources are located towards places with higher extinction (cf. Figs. 10 - 17, top panels). These properties agree well with previous findings in the W5 region (Koenig, Allen, Gutermuth et al. 2008; Deharveng, Zavagno, Anderson et al. 2012) and with the assumed evolutionary stages of both classes: the younger Class I sources are more clustered and associated with the most dense molecular material in which they were born,

while the Class II sources are scattered probably by moving away from their birthplaces. Chavarría, Allen, Brunt et al. (2014) showed that their samples of embedded clusters are likely gravitationally unbound, supporting the result that the more evolved members move further away due to the weak gravitational well of the cluster.

#### 4.1.2. Scattered YSOs population

Many ground-based near-IR surveys of molecular clouds (e.g., Lada, Bally, & Stark 1991; Strom, Strom, & Merrill 1993; Carpenter, Heyer, & Snell 2000; Porras, Christopher, Allen et al. 2003; Lada & Lada 2003) have shown that the molecular clouds contain both, a dense ‘clustered’ and a diffuse ‘distributed’ population. Koenig, Allen, Gutermuth et al. (2008) have analyzed the clustering properties of objects classified as young stars across the W5 region and found 40-70% of these sources belong to groups with  $\geq 10$  members and remaining were termed as scattered populations. Although the cluster cores of the BRCs have sizes of the order of a parsec (Miao, White, Nelson et al. 2006), the stars in them may have moved off from their formation site in few Myr. Weidner, Bonnell, & Moeckel (2011) using N-body calculations, studied the numbers and properties of escaping stars from low number ( $N=100$  and  $1000$ ) young embedded star clusters prior to gas expulsion over the first 5 Myr of their existence. They have found that these clusters can lose substantial amounts (upto 20%) of stars within 5 Myr. In the present sample of BRCs (except SFO 75), the cores have  $< 100$  stars as their members. These stars probably have mean velocity of  $\sim 2$  km s $^{-1}$  (Weidner, Bonnell, & Moeckel 2011) and can travel the distance of  $\sim 2 - 6$  pc during the 1-3 Myr of their formation (the typical age of the BRC YSOs: Chauhan, Pandey, Ogura et al. 2009, 2011; Panwar, Chen, Pandey et al. 2014). Therefore, for the  $\sim 10 \times 10$  arcmin square FOV of ISPI, we expect 5-10% of the stars would have escaped from the core region and are not included in our analyses. We have calculated the fraction of the scattered YSOs population (the YSOs outside the cores, but in the active regions) and found they are between  $\sim 20-45$  % of the total YSOs in the whole active region. Similar numbers have also been found in other studies also (30-50 % : Chavarría, Allen, Brunt et al.

2014). Out of these YSOs in the outer regions, 62 % are Class II objects, which is more or less similar to previous findings (cf. 67 % , Chavarría, Allen, Brunt et al. 2014). This higher percent of the comparatively older population in the outer regions is in accordance with their dynamical evolution. Chavarría, Allen, Brunt et al. (2014) have argued that the 10-20 % of the scattered population in their sample were the members of the cluster and happened to move away because of the dynamical relaxation. In addition to the above, the explanation of the scattered populations may include: dynamical interaction between cluster members, small groups merging, cluster definition and isolated star formation (for details, cf. Chavarría, Allen, Brunt et al. 2014).

#### 4.1.3. YSOs spacings

The complex patterns (e.g. filaments, bubbles and irregular clumps etc.) found in YSO population in SFRs are the result of the interplay of fragmentation process, turbulence, magnetic fields, crossing the Galactic arms’ potential, activities of massive stars in a region etc. Fragmentation of the gas with turbulence (e.g. Ballesteros-Paredes, Klessen, Mac Low et al. 2007, and refs. therein) and magnetic fields (e.g. Ward-Thompson, André, Crutcher et al. 2007, and refs. therein) have been discussed, leading to detailed predictions of the distributions of fragment spacings. Observations of SFRs (see Gutermuth, Megeath, Pipher et al. 2005; Teixeira, Lada, Young et al. 2006) suggest a strong peak in their histograms of NN spacings of the protostars in young embedded clusters. This peak indicates a significant degree of Jeans fragmentation, since this most frequent spacing agrees with an estimate of the Jeans length for the dense gas within which YSOs are embedded.

From the histograms (cf. Fig. 9) of NN2/NN6, it is clear that all the BRCs in the current sample have peaks at small spacings and they have a relatively long tail of large spacings. Although the peak may be sharp, or broad, or one of several near equivalent peaks, such a peaked character is often observed, regardless of the two dimensional distribution of sources (Gutermuth, Megeath, Myers et al. 2009). Peaked NN2 distance distributions typically suggest a significant subregion (or subregions) of relatively uni-

form, elevated surface density (Gutermuth, Megeath, Myers et al. 2009). Gutermuth, Megeath, Myers et al. (2009) in their study of 36 star-forming clusters, have also observed that short spacings are relatively more frequently than longer ones. Their sample shows a well defined peak at 0.02-0.05 pc and a tail extending to the spacings of 0.2 pc or greater. All the BRCs in the present study also show a well-defined single peak with extended spacing upto 1 pc in their respective histograms of NN2/NN6 distributions. Since NN2 is more sensitive to the local density fluctuations, it shows the median value of 0.03 pc over all BRCs for the peak of this distribution, whereas, NN6, which is an indicator of larger scale fluctuation, shows a comparatively larger peak value of 0.19 pc.

## 4.2. Physical properties of YSO cores and the active regions in the BRCs

In this Section, we investigate the physical properties of the identified active regions/cores in the present sample of BRCs.

### 4.2.1. Class I versus Class II distribution

We have calculated the median values of  $A_K$  as  $\sim 1.3$  mag and  $\sim 1.0$  mag and the YSOs separation as 0.07 pc and 0.11 pc for the Class I and Class II sources, respectively, in all cores of the studied BRCs. Similar values of these quantities have been found even for the active regions (cf. Table 6). Therefore, we can conclude that the Class I sources are located towards the places with higher extinction and are relatively closer to each other than the Class II sources (for details, see Table 6 and Figs. 10 - 17 (top left panels)). We have also calculated the fraction of the Class I objects among all the YSOs (cf. Table 4, last column) as an indicator of the "star formation age" of a region. The median values for this in the cores and in the active region are 66% and 52% (cf. Table 6), respectively. If we calculate this fraction only for the outer active region, excluding the inner cores, it falls to 38%. If we include only the YSOs being categorized by the *Spitzer* data (cf. Table 6), we still find a similar trend indicating higher percentages of younger sources in the inner regions of BRCs having high column densities. This is also in agreement with the conclusions of (Gutermuth, Megeath, Myers et al. 2009; Gutermuth, Pipher, Megeath et al. 2011) that

protostars are found in regions having marginally higher stellar surface densities than the more evolved PMS stars.

### 4.2.2. YSO surface densities

The YSOs in our cluster sample have mean surface densities mostly between 10 and 300  $\text{pc}^{-2}$  (see Table 5 and Fig. 19) for the cores and the active regions, respectively. These values are in agreement with the values given by Gutermuth, Megeath, Myers et al. (2009) for their sample of low-mass embedded clusters (LECs). The median values for the surface densities for the cores and the active region come out to be around 60  $\text{pc}^{-2}$  and 28  $\text{pc}^{-2}$ , respectively. The peak surface densities vary between 17 -1330  $\text{pc}^{-2}$  for our sample (cf. Table 5 and Fig. 19). Cores show a peak in the distribution of peak surface density at around 150  $\text{pc}^{-2}$  (cf. Fig. 19). Chavarría, Allen, Brunt et al. (2014) in their sample of embedded clusters found a weak trend between the peak surface density and the number of cluster members, suggesting that the clusters are better characterized by their peak YSOs surface density. In the present sample, the YSOs also follow a similar correlation (cf. Fig. 19).

### 4.2.3. Core morphology

The groups of young stars in SFRs show a wide range of sizes, morphologies and star numbers (cf. Gutermuth, Myers, Megeath et al. 2008; Gutermuth, Megeath, Myers et al. 2009; Gutermuth, Pipher, Megeath et al. 2011; Chavarría, Allen, Brunt et al. 2014). Recently Kuhn, Feigelson, Getman et al. (2014) studied 142 sub-clusters in different SFRs, and found their elongated morphologies with the core radius peaking at 0.17 pc. We use the clusters convex hull radius ( $R_H$ ) and aspect ratio to investigate their morphology (see Table 5 and Fig. 20). The  $R_H$  values of the cores range between 0.2 and 2.0 pc with a median value of 0.6 pc (cf. Table 6). These values are similar to those reported by Chavarría, Allen, Brunt et al. (2014) for a sample of LEC (0.5 pc). Most of the cores and active regions in the present sample are also found within a range of constant surface density of 12 - 300  $\text{pc}^{-2}$  (cf. Fig. 20), as reported by Gutermuth, Megeath, Myers et al. (2009). Almost all the cores in the present sample show an

elongated morphology with the median value of the aspect ratios around 1.45.

The median number of YSOs in cores and in active region are 35 and 97 (cf. Table 6), respectively, for the present sample of BRCs. The median MST branch length for these cores is found to be 0.09 pc. The total sum of YSOs in the active regions for all the BRCs is 997, out of which 602 (60%) falls in the cores. These numbers are very similar to those given in literature: 62% (Gutermuth, Megeath, Myers et al. 2009) and 66% (Chavarría, Allen, Brunt et al. 2014).

#### 4.2.4. Structural $Q$ parameter

The spatial distribution of YSOs associated with the BRCs is also investigated by their structural  $Q$  parameter values. The  $Q$  parameter (Cartwright & Whitworth 2004; Schmeja & Klessen 2006) is used to measure the level of hierarchical versus radial distributions of a set of points, and it is defined by the ratio of the MST normalized mean branch length and the normalized mean separation between points (cf. Chavarría, Allen, Brunt et al. 2014, for details). By using the normalized values, the  $Q$  parameter becomes independent from the cluster size (Schmeja & Klessen 2006). According to Cartwright & Whitworth (2004), a group of points distributed radially will have a high  $Q$  value ( $Q > 0.8$ ), while clusters with a more fractal distribution will have a low  $Q$  value ( $Q < 0.8$ ).

We find that our sample of BRCs has median  $Q$  values less than 0.8 (0.66 in cores and 0.70 in active regions, cf. Tables 5 and 6), showing a more fractal distribution especially in the inner regions of BRCs. Chavarría, Allen, Brunt et al. (2014) have found a weak trend in the distribution of  $Q$  values per number of members, suggesting a higher occurrence of sub-clusters merging in the most massive clusters, which decreases the value of the  $Q$  parameter. For our sample we didn't find any such correlation (cf. Fig. 21).

We compared the  $Q$  parameters for Class I and Class II sources (see Table 6), and found that the Class I sources are distributed more hierarchically than the Class II sources ( $Q_{\text{Class I}} < Q_{\text{Class II}}$ ). A similar result is shown by Chavarría, Allen, Brunt et al. (2014) and Schmeja, Kumar, & Ferreira (2008) for low-mass SFRs and is likely a consequence of the

cluster's dynamic relaxation.

#### 4.2.5. Associated molecular material

The mean  $A_K$  values for the identified cores have been found to be in between 0.5 and 1.6 mag, with a median value of 1.1 mag (cf. Table 6 and Fig. 22). This is very similar to the values given by Chavarría, Allen, Brunt et al. (2014) for LECs. However, the peak value of  $A_K$  (2.3 mag) for the current sample is higher than the value (1.5 mag) reported for LECs by Chavarría, Allen, Brunt et al. (2014). We have found a weak correlation between the peak  $A_K$  and the number of cluster members (cf. Fig. 22). The median  $A_K$  value for the whole active region is 0.8 mag, which is lower than the core value, naturally indicating the distribution of higher density of YSOs towards the high density molecular clouds.

#### 4.2.6. Jeans Length

Gutermuth, Megeath, Myers et al. (2009) analyzed the YSOs spacings of the YSOs in the stellar cores of 36 star-forming clusters and suggested that Jeans fragmentation is a starting point for understanding the primordial structure in SFRs. We have also calculated the minimum radius required for the gravitational collapse of a homogeneous isothermal sphere (Jeans length ' $\lambda_J$ ') in order to investigate the fragmentation scale by using the formulae given in Chavarría, Allen, Brunt et al. (2014).

The Jeans length  $\lambda_J$  for the cores in the current study has values between 0.2 - 1 pc, with a median value of 0.46 pc (cf. Tables 5 and 6). We have also compared  $\lambda_J$  and the mean separation ' $S_{YSO}$ ' between cluster members (Fig. 23) and found that the ratio  $\lambda_J/S_{YSO}$  has an average value of  $4.9 \pm 1.2$ . Similarly, Chavarría, Allen, Brunt et al. (2014) reported the ratio for their sample of embedded clusters as  $4.3 \pm 1.5$ . Present results agree with a non-thermal driven fragmentation since it took place at scales smaller than the Jeans length (Chavarría, Allen, Brunt et al. 2014).

#### 4.2.7. Molecular content

We have calculated the molecular mass of the identified cores/active regions using the extinction maps generated in the §3.3. First, we have

converted the average  $A_V$  value (corrected for the foreground extinction) in each grid of our map into  $H_2$  column density using the relation given by Dickman (1978); Cardelli, Clayton, & Mathis (1989), i.e.  $N(H_2) = 1.25 \times 10^{21} \times A_V \text{ cm}^{-2} \text{ mag}^{-1}$ . Then, this  $H_2$  column density has been integrated over the convex hull of each region and multiplied by the  $H_2$  molecule mass to get the molecular mass of the cloud. The extinction maps used for this are shown in Figs. 10 - 17. The extinction law,  $A_K/A_V = 0.090$  (Cohen, Persson, Elias et al. 1981) has been used to convert  $A_K$  values of our maps to  $A_V$ . Foreground contributions have been corrected by using the relation:  $A_{K_{foreground}} = 0.15 \times D$  (Indebetouw, Mathis, Babler et al. 2005,  $D$  is distance in kpc). The properties of the molecular clouds associated with the cores and active regions are listed in Table 5. The cores in the present sample show a wide range in their cloud mass distribution ( $\sim 20$  to  $2400 M_\odot$ ), with a median value around  $130 M_\odot$ .

Lada, Lombardi, & Alves (2010) found that the number of YSOs in a cluster are directly proportional to the dense cloud mass  $M_{0.8}$  (the mass above a column density equivalent to  $A_K \sim 0.8$  mag) with a slope equal to one. This gives an empirical relation between the content of YSOs and their parent molecular cloud. Recently, Chavarría, Allen, Brunt et al. (2014) have checked the same relation for their sample of embedded clusters and found a similar slope of  $0.89 \pm 0.15$  between the mass of the dense cloud and the number of cluster members. This suggests that the star formation rates depend linearly on the mass of the dense cloud (Lada, Lombardi, & Alves 2010). We have also calculated the  $M_{0.8}$  (cf. Table 5, as explained in Chavarría, Allen, Brunt et al. 2014) for our sample of BRCs. We find that the number of YSOs is proportional to  $M_{0.8}$  with a slope of 0.47 (cf. Fig. 24), which is very similar to the slope of 0.5, as calculated by Chavarría, Allen, Brunt et al. (2014), when they have not corrected their sample for the non-detection of fainter members. Once they applied the corrections for these non-detections, they found an almost similar slope ( $0.89 \pm 0.15$ ) as given by Lada, Lombardi, & Alves (2010). The data used and the distances of the present sample of BRCs (1 - 2.7 kpc) are more or less similar to

those embedded clusters (1.6 - 2.7 kpc) studied in Chavarría, Allen, Brunt et al. (2014). We therefore expect a similar level of non-detection for our sample. Hence, it may give a similar relation as that of Lada, Lombardi, & Alves (2010). In summary, we can at-least say that there is a linear relation between the dense cloud mass and the number of YSOs for the present sample of BRCs.

#### 4.2.8. Star formation efficiency

The wide range in observed YSO surface densities provides an opportunity to study how this quantity is related to the observed star formation efficiency (SFE) and the properties of the associated molecular cloud (Gutermuth, Pipher, Megeath et al. 2011). Recent works indicate that SFE increases with the stellar density. Evans, Dunham, Jørgensen et al. (2009) showed that YSO clusterings of higher surface density tend to exhibit higher SFE (30%) than their lower density surroundings (3%-6%). Koenig, Allen, Gutermuth et al. (2008) found SFEs of >10%-17% for high surface density clusterings and 3% for lower density regions.

We have calculated the SFE, defined as the percentage of gas mass converted into stars by using the cloud mass derived from  $A_K$  inside the cluster convex hull area and the number of YSOs found in the same area (see also Koenig, Allen, Gutermuth et al. 2008). For simplicity, we have assigned 0.5 solar mass (cf. Koenig, Allen, Gutermuth et al. 2008) to each of the identified YSOs and found SFEs between 3 and 30 % with an average of  $\sim 14$  %. Chavarría, Allen, Brunt et al. (2014) have obtained the SFE of a range of 3-45 % with an average 20 % for the sample of embedded clusters. Our results are comparable to those of Chavarría, Allen, Hora et al. (2008) for the S254 region (4-33 % range and 10 % average) with the exception of G192.54-0.15. Although the cluster G192.54-0.15 is located inside the H II region, S254 having distance of 2.4 kpc, these authors have concluded that it is located in the background of the complex at a distance 9 kpc, based on its kinematics using the rotational model from Brand & Blitz (1993). The SFE of G192.54-0.15 is 54% for the distance of 2.4 kpc then decreases to 1% if we adopt 9 kpc.

The present SFE values are in agreement with the efficiencies needed to go from the core mass

function to the initial mass function (e.g. 30 per cent in the Pipe nebula and 40 per cent in Aquila, from Alves, Lombardi, & Lada 2007; André, Men’shchikov, Bontemps et al. 2010, respectively). The SFE distribution as a function of the number of the cluster member of each region is shown in Fig. 25. There seem to be no correlation between them. This suggests that feedback processes may start having an impact only in the later stages of the cluster evolution

### 4.3. Biases

#### 4.3.1. Effect of uncertainty in distance on the analyses

Since, the distances of the BRCs studied in the present survey have been taken from the literature (cf. §1), which are essentially the photometric distances of the bright ionizing source(s) with typical uncertainties of the order of  $\sim 10\%$ , this will have corresponding effects on the various parameters given in Table 5 and Table 6. For example, as for  $R_{hull}$ ,  $R_{circ}$ ,  $\rho$ , MST/NN2 length and  $D_{crit.}$ , the dependence on the distance is simple and linear, therefore the percentage error associated with them due to the error in distance would be of the same order. The uncertainty due to it would be the largest in the derived mass, stellar density and SFE ( $\sim 20\%$ ), whereas the Jeans length would be in error by 15%. We have also plotted these errors in the Figs. 19, 20, 24 and 25. There are no significant changes in the distributions in the figures.

#### 4.3.2. Effect of non-detection of YSOs on the analyses

The detection of YSOs is affected by the presence of bright infrared sources, bright nebosity, and as well as by the high crowding in the BRCs, and we expect varying degrees of the detection completeness as a function of the above factors. To quantitatively analyze these effects, we followed the same approach as demonstrated by Chavarría, Allen, Brunt et al. (2014). Percentage of the corrected number of cluster members ( $N_{YSO}^*$ ) can be estimated from the equation given by Chavarría, Allen, Brunt et al. (2014) i.e.,

$$N_{YSO}^* = \frac{N_{YSO}/(1-IR)}{1-k},$$

where  $IR$  is the percentage of cluster mem-

bers without IR-excess and  $k$  is the percentage of synthetic stars with  $K$  magnitudes fainter than 90% completeness limit of a synthetic cluster having similar properties as the observed clusters. Chavarría, Allen, Brunt et al. (2014) found that  $k$  varies on average by 10% for their sample of embedded clusters. The percentage of cluster members without IR-excess in the present sample of BRC should be of the order of 10% (cf. §3.1). Therefore, the percentage of lost YSOs will be around 20% of the total YSOs identified in the present survey in each BRC. This bias will have a considerable effect on the reported peak YSO surface densities as well as on the higher density portions of the nearest neighbor surface density maps. We expect only a modest effect on the mean YSO surface densities and overall member counts. As the completeness decreases, we expect to lose preferentially those stars which are deeply embedded in the nebosity of the BRCs and most of them are likely of younger evolutionary class (Class I) located in the cores. Therefore, most probably, adding non-detected stars might complement some of the results in this study.

## 5. Conclusion

We carried out deep and wide field NIR observations of eight southern BRCs previously categorized as triggered candidates by Urquhart, Morgan, & Thompson (2009) using the ISPI camera on the 4m CTIO Blanco telescope. These data along with the *Spitzer* archive data have been used to identify deeply embedded low mass YSOs. Spatial distribution of these YSOs has been compared with their associated molecular clouds which have been inferred by the extinction analysis. Quantitative techniques have been used for analyzing the spatial structure of the YSO aggregates. The main results of our studies are as follows:

- We have identified a large number of YSOs, implying recent star formation in each of these BRCs. The number of the YSOs ranges from 44 to 433. This sample of YSOs is complete down to sub-solar masses. We have classified these YSOs based on their excess emission in IR.
- Isodensity contours of the YSOs and NIR extinction maps for the regions studied have



been generated and compared with those of other SFRs. The YSOs are generally distributed in groups in the regions of higher extinction, peaking at or near the peak of the molecular column density. A majority of younger population, i.e., Class I sources belong to these groups, whereas the comparatively older population, i.e., Class II objects, are more randomly distributed throughout the regions. This distribution is in accordance with the notion the star formation usually takes place inside the dense cores of the molecular clouds and the YSOs often follow their clumpy structures.

- 19-46 percent of the YSOs in the present sample of BRCs are a scattered population. Out of these, 62 percent are comparatively older Class II objects (cf. 38 percent in the cores). This higher percent in the outer regions can be attributed to their dynamical evolution.
- The concentrations of YSOs in our sample have similar projected NN spacings as in many other embedded cluster cores, having a well defined single peak which indicates a significant degree of Jeans fragmentation. NN2, being more sensitive to the local density fluctuations, shows a median value of 0.03 pc for the peak of their histogram, whereas, NN6, which is an indicator of larger scale fluctuation, shows a comparatively larger peak value (0.19 pc).
- The Class I sources are associated with higher extinction and are located relatively closer to each other than the Class II sources. Higher numbers of younger sources in the inner regions of BRCs having high column densities of molecular cloud confirm that the young protostars are usually found in regions having marginally higher surface densities than the more evolved PMS stars.
- MST analyses is used to isolate star forming stellar cores from a diffuse, sparsely distributed, and potentially varying density background. We have extracted thirteen stellar cores of eight or more members. The active regions in all the studied BRCs contain in total 997 YSOs, out of which 602

(60%) belong to the cores. The median MST branch length in these cores is found to be 0.09 pc. The members of these cores are mostly younger YSOs.

- Several basic structural measurements of these cores have been done, finding that the median core is 0.6 pc in radii and somewhat elongated (aspect ratio of 1.45), of relatively low density ( $60 \text{ pc}^2$ ), small (35 members), young (66% Class I), and partially embedded (median  $A_K = 1.1 \text{ mag}$ ).
- BRCs show fractal distribution of YSOs in their inner regions. Also, the Class I sources are distributed more hierarchically than the Class II, which is likely a consequence of the dynamical relaxation. The Jeans lengths for the cores have values between 0.2 - 1 pc, with a median value of 0.46 pc. Longer Jeans lengths in comparison to YSOs separations support the non-thermally driven fragmentation in the BRCs.
- The cores in the present sample show a wide range in their mass distribution ( $\sim 20$  to  $2400 M_\odot$ ) with a median value around  $130 M_\odot$ . We found a linear relation between the density of the clouds and the number of YSOs for the present sample of BRCs. We also found the SFEs for the identified cores to be between 3 and 30 % with an average of  $\sim 14$  %. These values are in support of the previous findings agreeing with the efficiencies needed to go from the core mass function to the initial stellar mass function.

## Acknowledgments

The observations reported in this paper were carried out by using the BLANCO telescope at CTIO. We thank the staff members for their assistance during the observations. Financial supports for J.B and R.K. are provided by the Ministry of Economy, Development, and Tourism's Millennium Science Initiative through grant IC120009, awarded to The Millennium Institute of Astrophysics, MAS. and Fondecyt Reg. No. 1130140 and 1120601. This work is based in part on data obtained by the *Spitzer* Space Telescope, which is operated by the Jet Propulsion Laboratory, Caltech, under a contract with NASA. Support to

this work was provided by NASA through a contract issued by JPL/Caltech. This publication also makes use of data from the Two Micron All Sky Survey, which is a joint project of the University of Massachusetts and the Infrared Processing and Analysis Center/California Institute of Technology, funded by the National Aeronautics and Space Administration and the National Science Foundation.

## REFERENCES

- Allen, L., Megeath, S. T., Gutermuth, R., et al. 2007, *Protostars and Planets V*, 361–376. [astro-ph/0603096](#)
- Allen, L. E., Myers, P. C., Di Francesco, J., et al. 2002, *ApJ*, 566, 993. [astro-ph/0110096](#)
- Allen, T. S., Pipher, J. L., Gutermuth, R. A., et al. 2008, *ApJ*, 675, 491. [0710.5488](#)
- Alves, J., Lombardi, M., & Lada, C. J. 2007, *A&A*, 462, L17. [astro-ph/0612126](#)
- André, P., Men'shchikov, A., Bontemps, S., et al. 2010, *A&A*, 518, L102. [1005.2618](#)
- Armitage, P. J., Clarke, C. J., & Palla, F. 2003, *MNRAS*, 342, 1139. [astro-ph/0303343](#)
- Ballesteros-Paredes, J., Klessen, R. S., Mac Low, M.-M., et al. 2007, *Protostars and Planets V*, 63–80. [arXiv:astro-ph/0603357](#)
- Baraffe, I., Chabrier, G., Allard, F., et al. 1998, *A&A*, 337, 403. [astro-ph/9805009](#)
- Bastian, N., Ercolano, B., Gieles, M., et al. 2007, *MNRAS*, 379, 1302. [0706.0495](#)
- Bastian, N., Gieles, M., Ercolano, B., et al. 2009, *MNRAS*, 392, 868. [0809.1943](#)
- Bate, M. R., & Bonnell, I. A. 2005, *MNRAS*, 356, 1201. [astro-ph/0411084](#)
- Bertoldi, F. 1989, *ApJ*, 346, 735
- Bessell, M. S., & Brett, J. M. 1988, *PASP*, 100, 1134
- Brand, J., & Blitz, L. 1993, *A&A*, 275, 67
- Cardelli, J. A., Clayton, G. C., & Mathis, J. S. 1989, *ApJ*, 345, 245
- Carpenter, J. M., Heyer, M. H., & Snell, R. L. 2000, *ApJS*, 130, 381. [astro-ph/0005237](#)
- Cartwright, A., & Whitworth, A. P. 2004, *MNRAS*, 348, 589. [astro-ph/0403474](#)
- Chauhan, N., Pandey, A. K., Ogura, K., et al. 2009, *MNRAS*, 396, 964. [0903.2122](#)
- Chauhan, N., Pandey, A. K., Ogura, K., et al. 2011, *MNRAS*, 415, 1202. [1103.3396](#)
- Chavarría, L., Allen, L., Brunt, C., et al. 2014, *MNRAS*, 439, 3719. [1403.3082](#)
- Chavarría, L. A., Allen, L. E., Hora, J. L., et al. 2008, *ApJ*, 682, 445. [0803.3358](#)
- Codella, C., Bachiller, R., Nisini, B., et al. 2001, *A&A*, 376, 271
- Cohen, J. G., Persson, S. E., Elias, J. H., et al. 1981, *ApJ*, 249, 481
- Deharveng, L., Zavagno, A., Anderson, L. D., et al. 2012, *A&A*, 546, A74. [1209.2907](#)
- Dickman, R. L. 1978, *ApJS*, 37, 407
- Evans, N. J., II, Dunham, M. M., Jørgensen, J. K., et al. 2009, *ApJS*, 181, 321. [0811.1059](#)
- Fazio, G. G., Hora, J. L., Allen, L. E., et al. 2004, *ApJS*, 154, 10. [astro-ph/0405616](#)
- Feigelson, E. D., & Montmerle, T. 1999, *ARA&A*, 37, 363
- Flaherty, K. M., Pipher, J. L., Megeath, S. T., et al. 2007, *ApJ*, 663, 1069. [astro-ph/0703777](#)
- Gomez, M., Hartmann, L., Kenyon, S. J., et al. 1993, *AJ*, 105, 1927
- Gutermuth, R. A., Megeath, S. T., Myers, P. C., et al. 2009, *ApJS*, 184, 18. [0906.0201](#)
- Gutermuth, R. A., Megeath, S. T., Pipher, J. L., et al. 2005, *ApJ*, 632, 397. [arXiv:astro-ph/0410750](#)
- Gutermuth, R. A., Myers, P. C., Megeath, S. T., et al. 2008, *ApJ*, 674, 336. [0710.1860](#)
- Gutermuth, R. A., Pipher, J. L., Megeath, S. T., et al. 2011, *ApJ*, 739, 84. [1107.0966](#)

- Haisch, K. E., Jr., Lada, E. A., & Lada, C. J. 2001, *ApJ*, 553, L153. [astro-ph/0104347](#)
- He, L., Whittet, D. C. B., Kilkenney, D., et al. 1995, *ApJS*, 101, 335
- Hernández, J., Hartmann, L., Calvet, N., et al. 2008, *ApJ*, 686, 1195. [0806.2639](#)
- Hillenbrand, L. A., Strom, S. E., Vrba, F. J., et al. 1992, *ApJ*, 397, 613
- Indebetouw, R., Mathis, J. S., Babler, B. L., et al. 2005, *ApJ*, 619, 931. [astro-ph/0406403](#)
- Jose, J., Pandey, A. K., Samal, M. R., et al. 2013, *MNRAS*, 432, 3445. [1304.5327](#)
- Koenig, X. P., Allen, L. E., Gutermuth, R. A., et al. 2008, *ApJ*, 688, 1142. [0808.3284](#)
- Kraus, A. L., Ireland, M. J., Hillenbrand, L. A., et al. 2012, *ApJ*, 745, 19. [1109.4141](#)
- Krumholz, M. R., & Tan, J. C. 2007, *ApJ*, 654, 304. [astro-ph/0606277](#)
- Kuhn, M. A., Feigelson, E. D., Getman, K. V., et al. 2014, *ApJ*, 787, 107. [1403.4252](#)
- Kumar, B., Sharma, S., Manfroid, J., et al. 2014, *A&A*, 567, A109. [1406.0994](#)
- Lada, C. J., Alves, J., & Lada, E. A. 1996, *AJ*, 111, 1964
- Lada, C. J., & Lada, E. A. 2003, *ARA&A*, 41, 57. [arXiv:astro-ph/0301540](#)
- Lada, C. J., Lombardi, M., & Alves, J. F. 2010, *ApJ*, 724, 687. [1009.2985](#)
- Lada, E. A., Bally, J., & Stark, A. A. 1991, *ApJ*, 368, 432
- Lefloch, B., & Lazareff, B. 1994, *A&A*, 289, 559
- Lefloch, B., Lazareff, B., & Castets, A. 1997, *A&A*, 324, 249
- Mallick, K. K., Ojha, D. K., Samal, M. R., et al. 2012, *ApJ*, 759, 48. [1209.3420](#)
- Marigo, P., Girardi, L., Bressan, A., et al. 2008, *A&A*, 482, 883. [0711.4922](#)
- Megeath, S. T., & Wilson, T. L. 1997, *AJ*, 114, 1106
- Meyer, M. R., Calvet, N., & Hillenbrand, L. A. 1997, *AJ*, 114, 288
- Miao, J., White, G. J., Nelson, R., et al. 2006, *MNRAS*, 369, 143. [astro-ph/0603230](#)
- Morgan, L. K., Thompson, M. A., Urquhart, J. S., et al. 2008, *A&A*, 477, 557. [0711.0775](#)
- Motte, F., Andre, P., & Neri, R. 1998, *A&A*, 336, 150
- Myers, P. C. 2009, *ApJ*, 706, 1341. [0910.3120](#)
- Ojha, D. K., Tamura, M., Nakajima, Y., et al. 2004a, *ApJ*, 616, 1042. [astro-ph/0408219](#)
- Ojha, D. K., Tamura, M., Nakajima, Y., et al. 2004b, *ApJ*, 608, 797. [arXiv:astro-ph/0403139](#)
- Pandey, A. K., Eswaraiah, C., Sharma, S., et al. 2013, *ApJ*, 764, 172. [1212.6706](#)
- Pandey, A. K., Sharma, S., Ogura, K., et al. 2008, *MNRAS*, 383, 1241. [0710.5429](#)
- Panwar, N., Chen, W. P., Pandey, A. K., et al. 2014, *MNRAS*, 443, 1614. [1406.6116](#)
- Phelps, R. L., & Janes, K. A. 1994, *ApJS*, 90, 31
- Porras, A., Christopher, M., Allen, L., et al. 2003, *AJ*, 126, 1916. [astro-ph/0307510](#)
- Povich, M. S., Smith, N., Majewski, S. R., et al. 2011, *ApJS*, 194, 14. [1103.2060](#)
- Robitaille, T. P., Meade, M. R., Babler, B. L., et al. 2008, *AJ*, 136, 2413. [0809.1654](#)
- Robitaille, T. P., Whitney, B. A., Indebetouw, R., et al. 2006, *ApJS*, 167, 256. [arXiv:astro-ph/0608234](#)
- Sagar, R., & Richtler, T. 1991, *A&A*, 250, 324
- Schmeja, S., Gouliermis, D. A., & Klessen, R. S. 2009, *ApJ*, 694, 367. [0812.3080](#)
- Schmeja, S., & Klessen, R. S. 2006, *A&A*, 449, 151. [astro-ph/0511448](#)
- Schmeja, S., Kumar, M. S. N., & Ferreira, B. 2008, *MNRAS*, 389, 1209. [0805.2049](#)
- Sharma, S., Pandey, A. K., Ogura, K., et al. 2008, *AJ*, 135, 1934. [0803.0122](#)

- Sharma, S., Pandey, A. K., Ojha, D. K., et al. 2007, MNRAS, 380, 1141. 0707.0269
- Sharma, S., Pandey, A. K., Pandey, J. C., et al. 2012, PASJ, 64, 107. 1204.2897
- Sharpless, S. 1959, ApJS, 4, 257
- Siess, L., Dufour, E., & Forestini, M. 2000, A&A, 358, 593. arXiv:astro-ph/0003477
- Stern, D., Eisenhardt, P., Gorjian, V., et al. 2005, ApJ, 631, 163. astro-ph/0410523
- Stetson, P. B. 1994, PASP, 106, 250
- Strom, K. M., Strom, S. E., Edwards, S., et al. 1989, AJ, 97, 1451
- Strom, K. M., Strom, S. E., & Merrill, K. M. 1993, ApJ, 412, 233
- Sugitani, K., Fukui, Y., & Ogura, K. 1991, ApJS, 77, 59
- Sugitani, K., & Ogura, K. 1994, ApJS, 92, 163
- Teixeira, P. S., Lada, C. J., Young, E. T., et al. 2006, ApJ, 636, L45. arXiv:astro-ph/0511732
- Thompson, M. A., & White, G. J. 2004, A&A, 419, 599. astro-ph/0402552
- Urquhart, J. S., Morgan, L. K., & Thompson, M. A. 2009, A&A, 497, 789. 0902.4751
- Urquhart, J. S., Thompson, M. A., Morgan, L. K., et al. 2004, A&A, 428, 723. astro-ph/0408205
- Urquhart, J. S., Thompson, M. A., Morgan, L. K., et al. 2006, A&A, 450, 625. astro-ph/0601718
- Urquhart, J. S., Thompson, M. A., Morgan, L. K., et al. 2007, A&A, 467, 1125. astro-ph/0703252
- van der Blik, N. S., Norman, D., Blum, R. D., et al. 2004, in Ground-based Instrumentation for Astronomy, Society of Photo-Optical Instrumentation Engineers (SPIE) Conference Series, vol. 5492, eds. A. F. M. Moorwood, & M. Iye, 1582–1589
- Ward-Thompson, D., André, P., Crutcher, R., et al. 2007, Protostars and Planets V, 33–46. arXiv:astro-ph/0603474
- Weidner, C., Bonnell, I. A., & Moeckel, N. 2011, MNRAS, 410, 1861. 1008.4578
- Winston, E., Megeath, S. T., Wolk, S. J., et al. 2007, ApJ, 669, 493. 0707.2537
- Yamaguchi, R., Saito, H., Mizuno, N., et al. 1999, PASJ, 51, 791
- Zinnecker, H., McCaughrean, M. J., & Wilking, B. A. 1993, in Protostars and Planets III, eds. E. H. Levy, & J. I. Lunine, 429–495

Table 1: Regions observed in the present study. The last column gives the stellar mass at the completeness limit of YSO detection after correcting for foreground and peak (in parenthesis) extinction values (cf. §3.2).

Name	$\alpha_{(2000)}$ ( $h:m:s$ )	$\delta_{(2000)}$ ( $o:l''$ )	$l$	$b$ (degrees)	Distance (kpc)	Pixel size (pc)	90% Completeness Limit ( $M_{\odot}$ )
SFO 54	08:35:31.7	-40:38:28	259.941383	-0.040549	0.95	0.0014	0.04(0.15)
SFO 55	08:41:13.0	-40:52:03	260.775002	0.678340	1.15	0.0017	0.03(0.10)
SFO 64	11:12:18.0	-58:46:20	290.374065	1.661209	2.70	0.0040	0.40(1.40)
SFO 65	11:33:00.0	-63:27:20	294.301328	-1.905817	1.70	0.0025	0.08(0.20)
SFO 68	11:35:31.9	-63:14:51	294.511530	-1.623458	1.70	0.0025	0.08(0.20)
SFO 75	15:55:50.4	-54:38:58	327.573745	-0.851722	2.80	0.0041	0.80(3.00)
SFO 76	16:10:38.6	-49:05:52	332.956319	1.803776	1.80	0.0027	0.15(1.40)
SFO 79	16:40:00.1	-48:51:45	336.491077	-1.475060	1.35	0.0020	0.10(2.00)
Field 1	08:34:42.4	-40:40:45	259.878445	-0.188092	--		
Field 2	16:39:03.7	-48:51:34	336.390516	-1.357565	--		

Table 2: Color coefficients and constants derived by using 2MASS data for the calibration of ISPI data. ‘N’ represents the total number of the common stars used in the fitting.

ID	N	$M1$	$C1$	$M2$	$C2$	$M3$	$C3$
SFO 54	220	$1.013 \pm 0.013$	$-0.077 \pm 0.020$	$0.963 \pm 0.026$	$0.420 \pm 0.005$	$-0.079 \pm 0.025$	$0.522 \pm 0.012$
SFO 55	223	$0.997 \pm 0.013$	$-0.038 \pm 0.020$	$0.996 \pm 0.027$	$0.460 \pm 0.005$	$-0.070 \pm 0.025$	$0.532 \pm 0.011$
SFO 64	617	$1.003 \pm 0.008$	$-0.086 \pm 0.008$	$0.952 \pm 0.017$	$0.427 \pm 0.005$	$-0.078 \pm 0.021$	$0.472 \pm 0.005$
SFO 65	671	$0.993 \pm 0.007$	$-0.008 \pm 0.009$	$0.943 \pm 0.026$	$0.449 \pm 0.004$	$-0.078 \pm 0.015$	$0.516 \pm 0.006$
SFO 68	672	$1.015 \pm 0.006$	$0.012 \pm 0.008$	$0.967 \pm 0.014$	$0.461 \pm 0.003$	$-0.065 \pm 0.016$	$0.501 \pm 0.005$
SFO 75	955	$0.986 \pm 0.006$	$0.079 \pm 0.011$	$0.946 \pm 0.010$	$0.596 \pm 0.002$	$-0.064 \pm 0.014$	$0.374 \pm 0.009$
SFO 76	993	$0.981 \pm 0.006$	$0.058 \pm 0.010$	$0.952 \pm 0.011$	$0.559 \pm 0.002$	$-0.069 \pm 0.014$	$0.554 \pm 0.008$
SFO 79	775	$0.991 \pm 0.005$	$0.002 \pm 0.010$	$0.970 \pm 0.010$	$0.458 \pm 0.003$	$-0.048 \pm 0.011$	$0.499 \pm 0.006$
Field 1	263	$1.009 \pm 0.013$	$-0.044 \pm 0.014$	$0.985 \pm 0.036$	$0.439 \pm 0.008$	$-0.089 \pm 0.034$	$0.490 \pm 0.010$
Field 2	1366	$0.990 \pm 0.004$	$-0.065 \pm 0.008$	$0.928 \pm 0.010$	$0.452 \pm 0.002$	$-0.052 \pm 0.007$	$0.502 \pm 0.007$

Table 3: Sample of YSOs identified in the present study on the basis of their excess IR-emission using CTIO/*Spitzer* data. Their respective magnitudes and photometric errors are also given. The last column gives the information about the scheme used in their classification. The complete table is available in the electronic form only.

Name (BRC-ID)	$\alpha_{(2000)}$ ( $h:m:s$ )	$\delta_{(2000)}$ ( $o:l''$ )	$J \pm \sigma$ (mag)	$H \pm \sigma$ (mag)	$K \pm \sigma$ (mag)	$3.6 \pm \sigma$ (mag)	$4.5 \pm \sigma$ (mag)	$5.8 \pm \sigma$ (mag)	$8.0 \pm \sigma$ (mag)	comment
SFO54_1	08:35:40.30	40:40:07.2	$9.704 \pm 0.017$	$8.880 \pm 0.019$	$8.128 \pm 0.015$	$7.191 \pm 0.110$	$6.818 \pm 0.070$	$6.135 \pm 0.018$	$5.430 \pm 0.046$	2
SFO54_2	08:35:32.82	40:38:36.2	–	$11.049 \pm 0.033$	$9.421 \pm 0.022$	$7.890 \pm 0.061$	$7.385 \pm 0.036$	$6.926 \pm 0.019$	$6.436 \pm 0.023$	2,6
SFO54_3	08:35:30.95	40:38:26.7	–	$13.023 \pm 0.067$	$9.865 \pm 0.033$	–	–	–	–	6
SFO54_4	08:35:22.56	40:38:50.2	$12.684 \pm 0.024$	$11.081 \pm 0.051$	$9.927 \pm 0.039$	$8.357 \pm 0.079$	$7.842 \pm 0.035$	$7.365 \pm 0.022$	$6.574 \pm 0.022$	2,5
SFO54_5	08:35:31.03	40:38:22.3	$14.586 \pm 0.004$	$12.171 \pm 0.005$	$10.523 \pm 0.016$	–	–	–	–	5
SFO54_6	08:35:17.76	40:38:23.4	$12.290 \pm 0.006$	$11.420 \pm 0.005$	$10.932 \pm 0.007$	$10.499 \pm 0.068$	$10.097 \pm 0.051$	$9.795 \pm 0.031$	$9.087 \pm 0.042$	2
SFO54_7	08:35:32.80	40:38:15.5	$13.628 \pm 0.002$	$11.964 \pm 0.002$	$11.095 \pm 0.004$	$9.773 \pm 0.086$	$9.222 \pm 0.050$	$8.507 \pm 0.036$	$7.732 \pm 0.023$	2
SFO54_8	08:35:34.65	40:37:27.3	$15.692 \pm 0.009$	$12.856 \pm 0.002$	$11.156 \pm 0.006$	$9.573 \pm 0.068$	$9.006 \pm 0.020$	$8.486 \pm 0.034$	$7.597 \pm 0.017$	2,5
SFO54_9	08:35:42.10	40:38:05.1	$13.125 \pm 0.002$	$12.003 \pm 0.002$	$11.227 \pm 0.006$	$10.383 \pm 0.070$	$10.400 \pm 0.039$	$10.311 \pm 0.042$	$10.220 \pm 0.031$	5
SFO54_10	08:35:25.92	40:38:58.3	$13.164 \pm 0.003$	$12.040 \pm 0.002$	$11.419 \pm 0.002$	$10.385 \pm 0.042$	$9.887 \pm 0.035$	$9.362 \pm 0.038$	$8.462 \pm 0.025$	2

\* 1=Class I (Through *Spitzer* data), 2=Class II (Through *Spitzer* data), 3=Class I (Through CTIO/*Spitzer* data), 4=Class II (Through CTIO/*Spitzer* data), 5=Class II (Through CTIO data), 6=Class I (Through CTIO data)

Table 4: Center coordinates of the identified cores and active regions along with the total number of the YSOs, and their distribution as a function of their evolutionary status. The numbers in bracket represent the YSOs classified by using the *Spitzer* IRAC data.

Name	$\alpha_{(2000)}$ ( <i>h.m.s</i> )	$\delta_{(2000)}$ ( <i>o.'''</i> )	N	Class I	Class II	Frac <sup>a</sup> (%)
Cores						
SFO 54 C1	08:35:28.6	-40:38:30	81	36( 3)	45(22)	44(12)
SFO 55 C1	08:41:13.5	-40:52:11	55	37( 4)	18(12)	67(25)
SFO 64 C1	11:12:19.1	-58:46:23	78	41( 1)	37(12)	53( 8)
SFO 65 C1	11:33:00.4	-63:28:16	21	15( 0)	6( 2)	71( 0)
SFO 68 C1	11:35:31.7	-63:14:58	35	23( 2)	12( 2)	66(50)
SFO 68 C2	11:34:58.5	-63:16:45	17	10( 0)	7( 0)	59( -)
SFO 75 C1	15:55:49.2	-54:39:15	175	114( 4)	61( 8)	65(33)
SFO 75 C2	15:56:12.3	-54:39:57	42	34( 0)	8( 0)	81( -)
SFO 76 C1	16:10:39.1	-49:06:53	30	21( 0)	9( 0)	70( -)
SFO 76 C1	16:10:25.5	-49:02:55	8	0( 0)	8( 0)	-( -)
SFO 79 C1	16:40:01.3	-48:51:43	84	53( 8)	31(15)	63(35)
SFO 79 C2	16:39:46.3	-48:51:05	11	10( 0)	1( 1)	91( 0)
SFO 79 C3	16:40:11.3	-48:48:59	25	17( 2)	8( 4)	68(33)
Active regions						
SFO 54 A	08:35:31.1	-40:38:43	128	48( 4)	80(45)	38( 8)
SFO 55 A	08:41:13.0	-40:52:27	78	49( 6)	29(19)	63(24)
SFO 64 A	11:12:21.1	-58:46:20	115	45( 2)	70(39)	39( 5)
SFO 65 A	11:32:49.4	-63:28:23	35	19( 0)	16( 5)	54( 0)
SFO 68 A	11:35:30.8	-63:13:59	97	50( 3)	47(11)	52(21)
SFO 75 A	15:55:54.4	-54:39:16	269	181( 4)	88(10)	67(29)
SFO 76 A	16:10:33.9	-49:05:56	56	26( 0)	30( 0)	46( -)
SFO 79 A	16:40:00.6	-48:51:31	219	155(12)	64(35)	71(26)

a: Class 1/(Class 1 + Class II)

Table 5: Properties of the identified cores and active regions. The hull and circle radius along with the aspect ratio are given in columns 2, 3 and 4, respectively. Columns 5 and 6 represent the mean and peak stellar density obtained using the isodensity contours. Columns 7 and 8 are the mean MST branch length and NN distances, respectively. The mean and peak extinction values are given in Columns 9 and 10, respectively. Column 11 represents the cloud mass in the convex hull derived using the extinction maps. Column 12 represents the mass of the dense cloud having  $A_K$  greater than 0.8 mag. Columns 13, 14 and 15 represent the  $Q$  value, Jeans length and critical branch length for MST, respectively.

Name	$R_{\text{hull}}$	$R_{\text{cir}}$	Aspect	$\rho_{\text{mean}}$	$\rho_{\text{peak}}$	MST	NN2	$A_{K_{\text{mean}}}$	$A_{K_{\text{peak}}}$	$M_{A_K}$	$M_{A_K}$	$Q$	J	$D_{\text{crit.}}$
	(pc)	(pc)	Ratio	( $\text{pc}^{-2}$ )	( $\text{pc}^{-2}$ )	(pc)	(pc)	(mag)	(mag)	( $M_{\odot}$ )	( $M_{\odot}$ )		(pc)	(pc)
Cores														
SFO 54 C1	0.40	0.45	1.28	163.21	1330.4	0.04	0.03	1.32	2.34	131.3	125.3	0.75	0.30	0.12
SFO 55 C1	0.58	0.70	1.49	52.83	454.1	0.07	0.06	1.09	1.89	215.3	189.5	0.64	0.46	0.18
SFO 64 C1	0.58	0.73	1.59	75.11	386.9	0.06	0.05	0.61	1.81	127.2	37.2	0.65	0.52	0.18
SFO 65 C1	1.02	1.29	1.58	6.38	17.1	0.20	0.12	0.65	1.97	296.9	168.8	0.59	0.98	0.56
SFO 68 C1	0.30	0.34	1.22	120.36	693.6	0.06	0.04	1.36	2.56	68.5	63.5	0.75	0.27	0.15
SFO 68 C2	0.30	0.28	0.89	61.15	132.0	0.09	0.03	0.49	1.12	19.8	2.6	0.66	0.46	0.15
SFO 75 C1	1.85	2.22	1.43	16.20	209.7	0.13	0.10	1.06	2.54	2416.1	2015.7	0.69	0.84	0.30
SFO 75 C2	0.81	0.83	1.07	20.61	86.4	0.11	0.09	1.50	2.73	525.9	517.5	0.67	0.52	0.30
SFO 76 C1	0.77	1.04	1.81	16.06	53.6	0.16	0.10	1.07	2.36	372.7	316.8	0.55	0.57	0.37
SFO 76 C1	0.37	0.36	0.96	18.76	26.5	0.19	0.15	0.56	0.86	27.0	2.2	0.71	0.65	0.37
SFO 79 C1	0.61	0.73	1.45	331.86	258.0	0.07	0.04	1.55	2.79	353.6	349.8	0.58	0.39	0.16
SFO 79 C2	0.18	0.24	1.69	104.62	150.0	0.07	0.06	1.64	2.20	21.5	21.5	0.62	0.23	0.16
SFO 79 C3	0.36	0.45	1.55	60.39	136.2	0.11	0.05	1.47	2.71	92.4	91.2	0.67	0.34	0.16
Active regions														
SFO 54 A	0.87	1.05	1.44	53.06	1330.4	0.06	0.05	0.91	2.34	451.8	299.0	0.85	0.57	0.26
SFO 55 A	0.85	1.00	1.39	34.37	454.1	0.09	0.06	1.03	1.89	465.3	393.1	0.70	0.57	0.29
SFO 64 A	1.15	1.52	1.74	27.75	386.9	0.09	0.06	0.42	1.81	348.3	63.6	0.80	0.97	0.40
SFO 65 A	1.62	1.68	1.07	4.24	17.1	0.32	0.15	0.54	1.97	800.1	200.3	0.69	1.21	0.84
SFO 68 A	0.88	1.35	2.36	39.72	693.6	0.07	0.05	0.76	2.56	391.3	255.6	0.59	0.63	0.30
SFO 75 A	2.63	3.22	1.50	12.42	209.7	0.16	0.11	1.12	2.84	5286.7	4601.4	0.71	0.97	0.40
SFO 76 A	1.66	1.87	1.26	6.47	53.6	0.19	0.15	0.67	2.36	1108.5	427.3	0.72	1.06	0.56
SFO 79 A	1.35	1.66	1.52	38.30	258.0	0.09	0.06	1.40	2.80	1683.8	1619.9	0.67	0.61	0.24

Table 6: Median averaged parameters of all the cores and active region. The figure in brackets represent the numbers of the YSOs classified by using the *Spitzer* IRAC data.

Properties	Core	Active region
Fraction of Class I sources (%)	66(33)	52(21)
NN2( <i>Class I</i> ) (pc)	0.07	0.07
NN2( <i>Class II</i> ) (pc)	0.10	0.11
$A_K$ ( <i>Class I</i> ) (mag)	1.3	1.1
$A_K$ ( <i>Class II</i> ) (mag)	1.0	0.8
Number of YSOs	35	97
$R_{\text{hull}}$ (pc)	0.58	1.15
Aspect Ratio	1.45	1.44
Mean number density ( $\text{pc}^{-2}$ )	60	28
Peak number density ( $\text{pc}^{-2}$ )	150	258
$A_K$ (mag)	1.1	0.8
Peak $A_K$ (mag)	2.3	2.3
Cloud mass ( $M_{\odot}$ )	131	465
Dense cloud mass ( $M_{\odot}$ )	125	299
MST branch length (pc)	0.09	0.09
Structural $Q$ parameter	0.66	0.70
Structural $Q$ parameter( <i>Class I</i> )	0.68	0.64
Structural $Q$ parameter( <i>Class II</i> )	0.72	0.81
Jeans Length (pc)	0.46	0.63
Star formation efficiency (%)	12	6

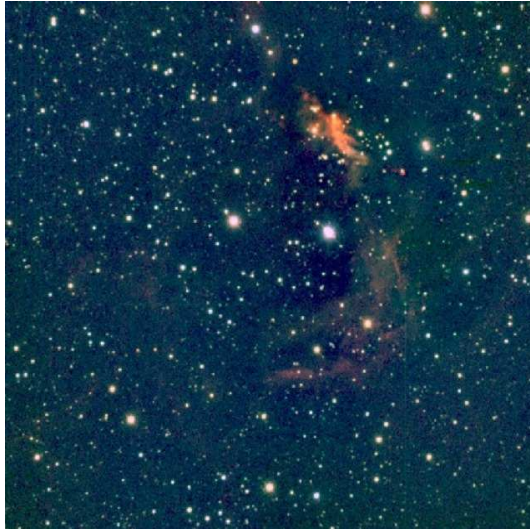


Fig. 1.— Color composite image of the SFO 54 region covering  $10 \times 10$  arcmin<sup>2</sup> FOV based on the ISPI data. The red, green and blue colors correspond to  $K'$ ,  $H$  and  $J$  bands, respectively.



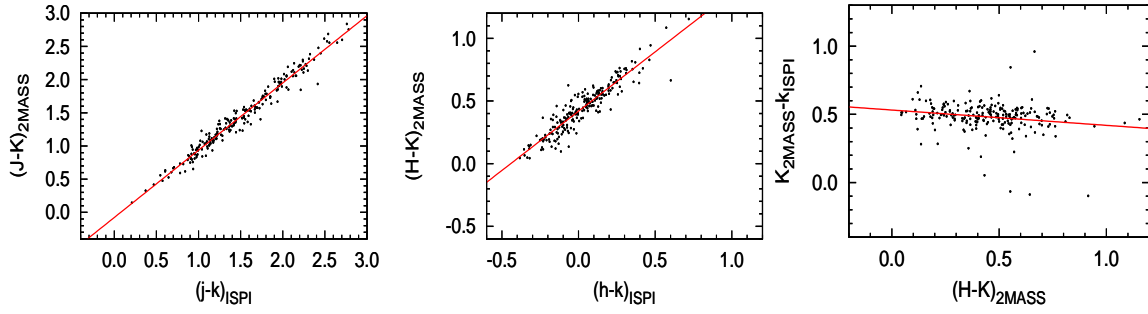


Fig. 2.— Fit for the transformation coefficients for ISPI data using 2MASS data for the sources in the SFO 54 region.

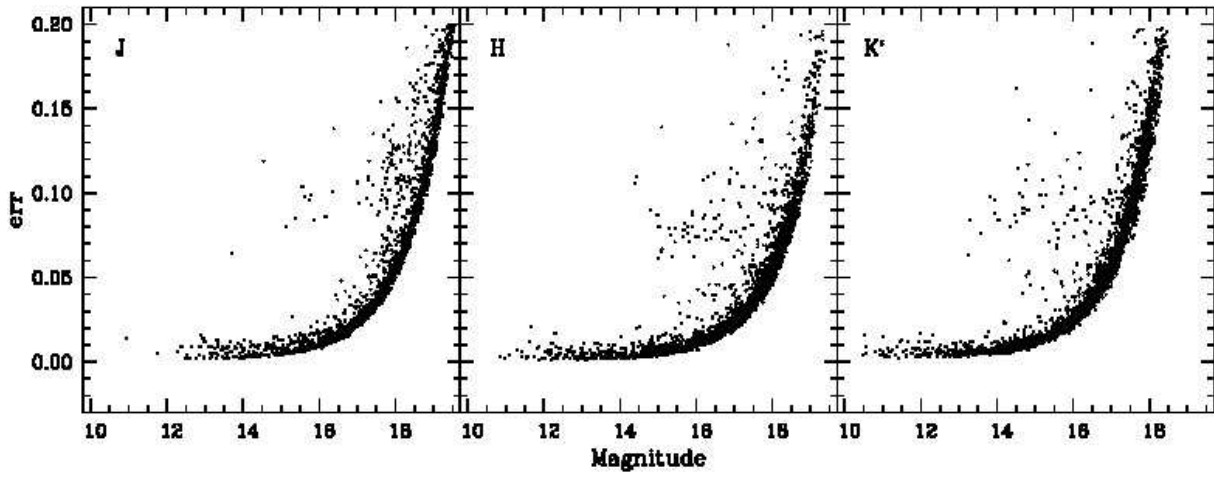


Fig. 3.— Photometric errors as a function of magnitudes for all three bands of ISPI data for the sources in the SFO 54 region.

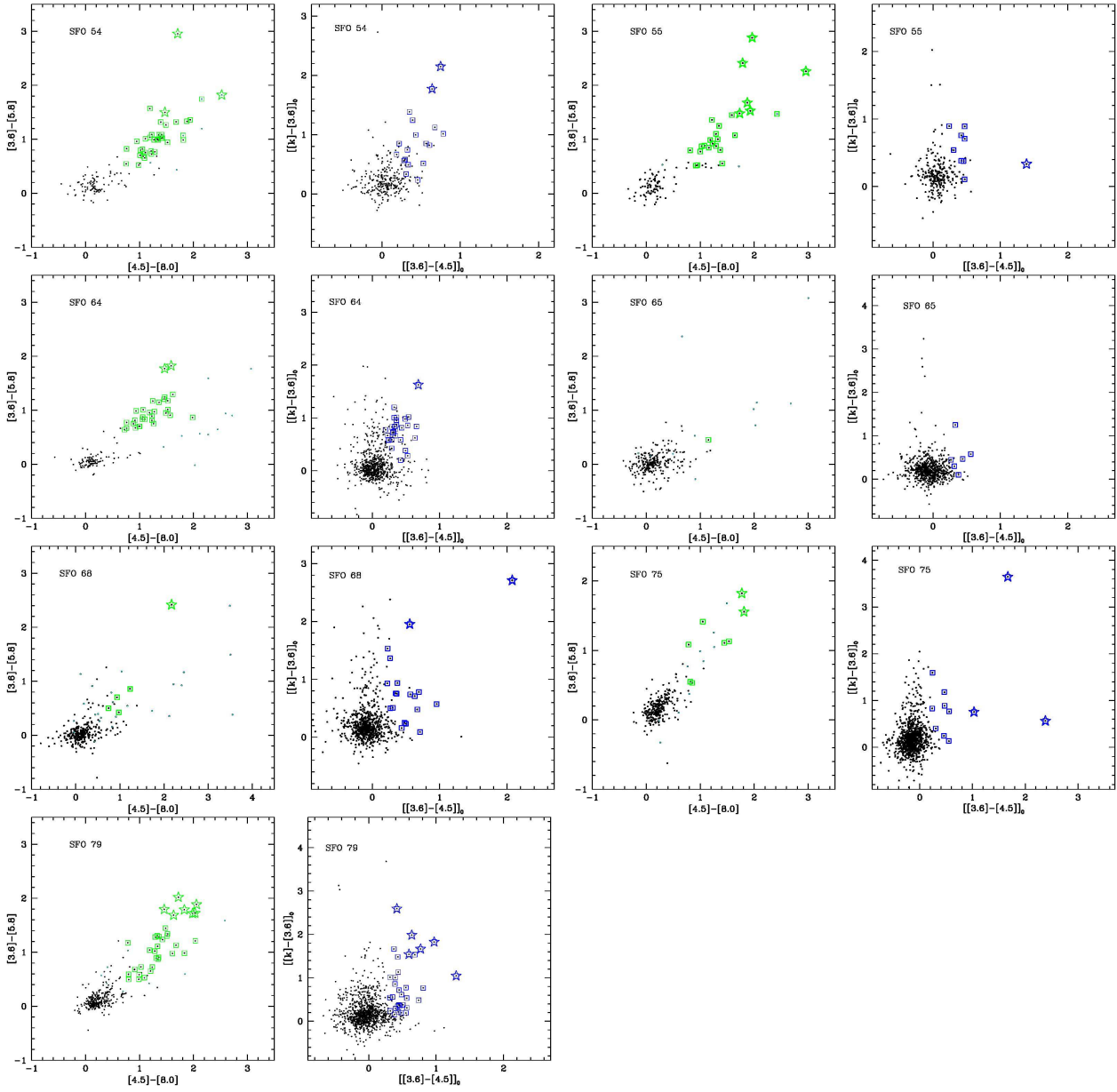


Fig. 4.— IRAC/2MASS TCDs for the stars in all the regions studied. The YSOs classified as Class I and Class II, based on the color criteria by Gutermuth, Megeath, Myers et al. (2009), are marked using star and square symbols, respectively.

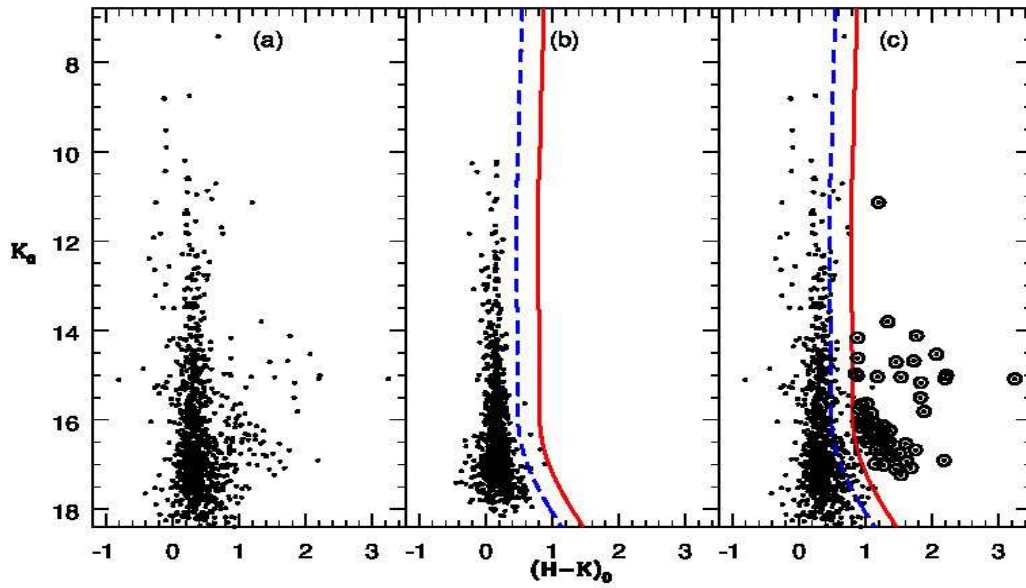


Fig. 5.—  $K_0/(H - K)_0$  CMD for (a) stars in the SFO 55 region, (b) stars in the field region and (c) stars in the SFO 55 region with the marked probable IR excess sources (circles). The blue dashed curve is the outer envelop of the dereddened field stars and the thick red curve separates the distribution of probable IR excess stars from that of MS stars.

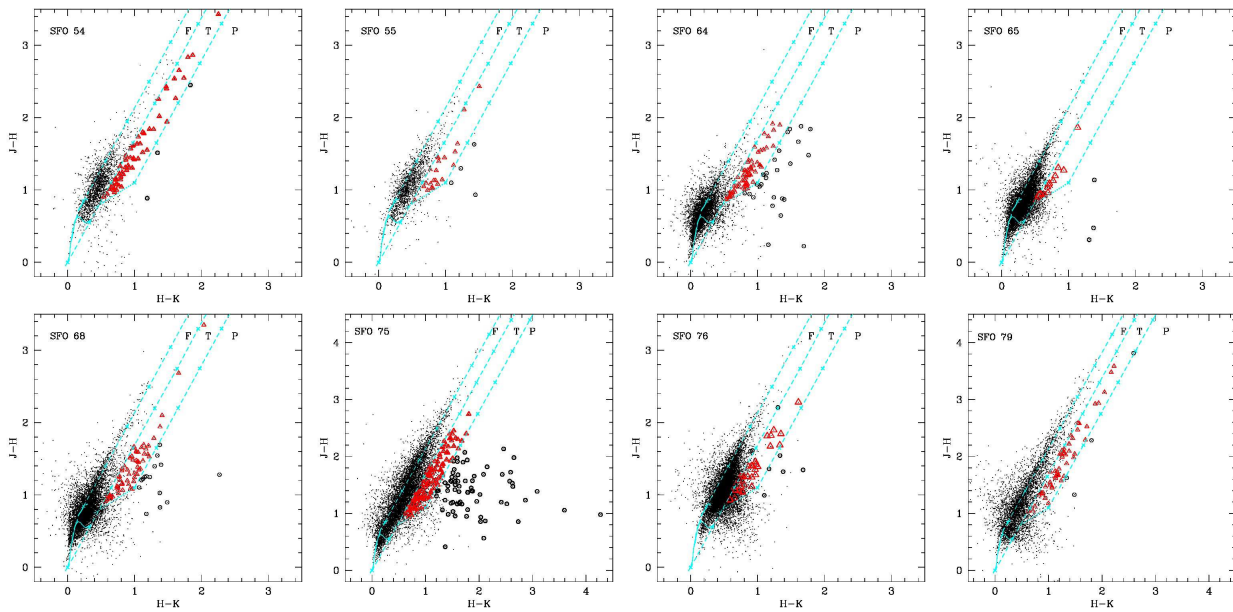


Fig. 6.— NIR TCD for the stars in all regions studied. The continuous and thick dashed curves represent the unreddened MS and giant branch (Bessell & Brett 1988), respectively. The dotted line indicates the loci of unreddened CTTSs (Meyer, Calvet, & Hillenbrand 1997). The parallel dashed lines are the reddening vectors drawn from the tip (spectral type M4) of the giant branch (left reddening line), from the base (spectral type A0) of the MS branch (middle reddening line) and from the tip of the intrinsic CTTS line (right reddening line). The crosses on the reddening vectors show an increment of  $A_V = 5$  mag. The sources marked with open triangles and circles are identified CTTSs and probable IR excess sources, respectively.

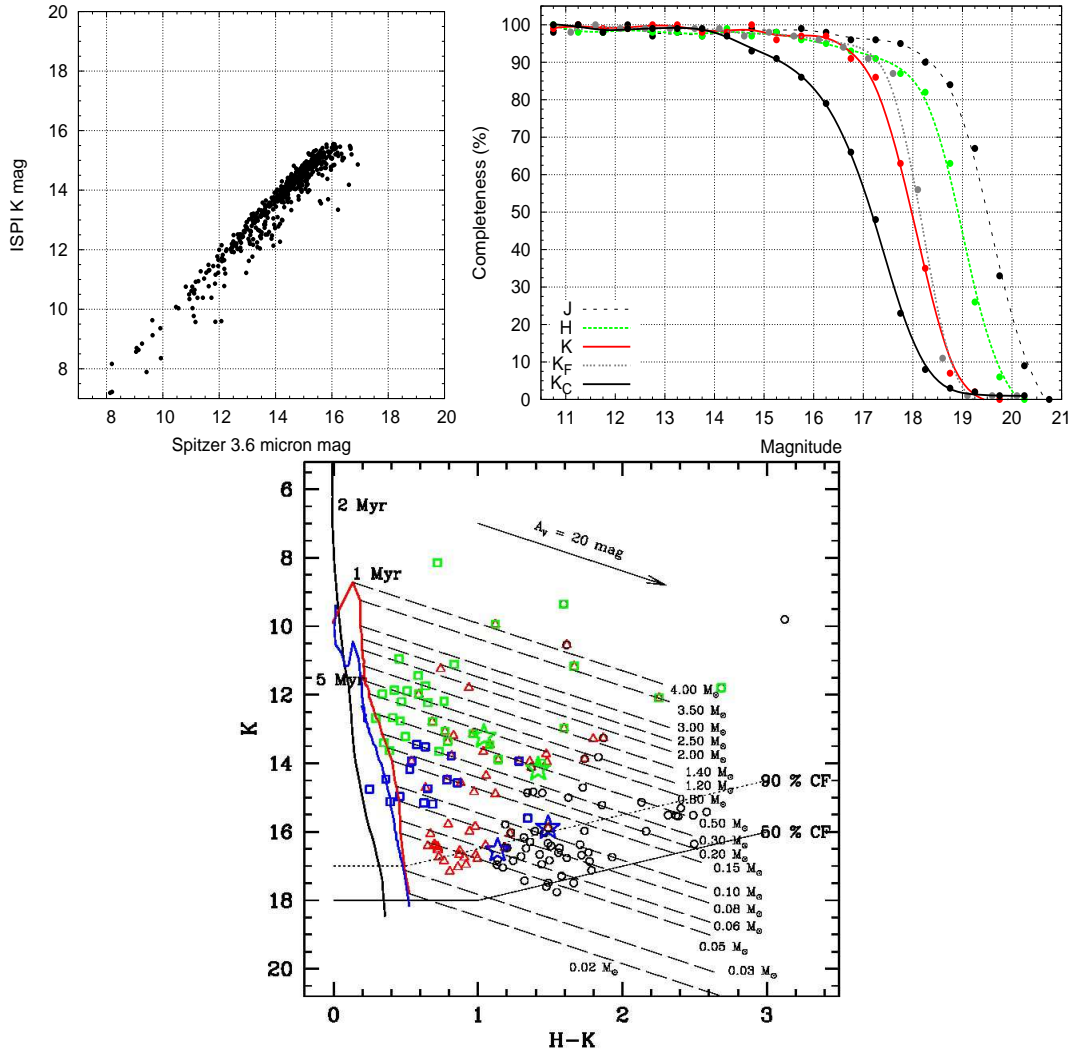


Fig. 7.— (Top Left): Comparison between the ISPI  $K$  band and *Spitzer*  $3.6 \mu\text{m}$  photometry. (Top Right): Completeness factor of the photometry in different ISPI bands in the SFO 54 region. Black dashed, dotted green and solid red curves are the smoothed bezier curves for the data points for completeness in the  $J$ ,  $H$  and  $K$  bands, respectively.  $K_F$  (dotted grey curve) and  $K_C$  (solid black curve) represent similar curves in  $K$  band for the field and SFO 64 regions, respectively. (Lower Panel):  $K$  vs  $(H - K)$  CMD for the YSOs detected in the SFO 54 region along with the theoretical MS isochrone of 2 Myr ( $Z = 0.02$ , solid black curve) by Marigo, Girardi, Bressan et al. (2008), and the PMS isochrones of ages 1 and 5 Myr (solid red and solid blue curves) by Siess, Dufour, & Forestini (2000) (for masses  $> 1.2 M_\odot$ ) and Baraffe, Chabrier, Allard et al. (1998) (for masses  $< 1.2 M_\odot$ ), all corrected for the distance and the foreground reddening. The symbols are same as in Figs. 4, 5 and 6. Slanting parallel dashed lines show the reddening vectors for PMS stars of different masses. The dotted and solid broken lines represent the 90% and 50% completeness limits for the data. See §3.2 for a detail.

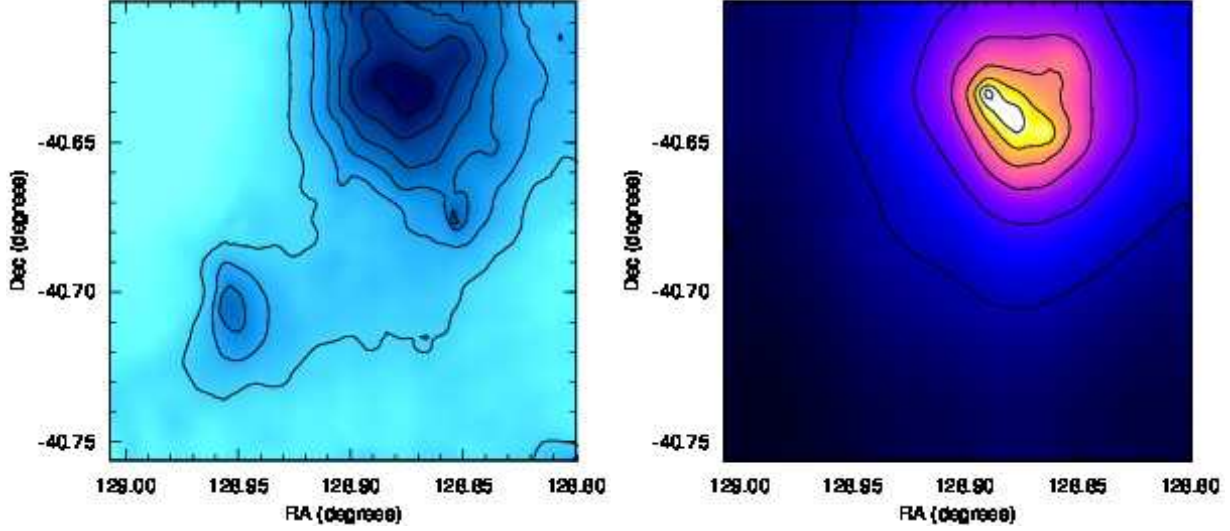


Fig. 8.— (Left Panel): Extinction map smoothed to a resolution of 5 arcsec for the SFO 54 region. The contours are drawn with a step size of  $A_K = 0.1$  mag starting from the lowest contour approximately equal to the mean  $A_K$  value for the selected active region (cf. Table 5). (Right Panel): Surface isodensity contours of YSOs detected in the same region with the same resolution. The contours are shown with a step size of 2 stars/arcmin<sup>2</sup> with the lowest contour approximately equal to the mean number density in arcmin square for the selected active region (cf. Table 5). Both the maps have FOV of  $\sim 10 \times 10$  arcmin<sup>2</sup>.

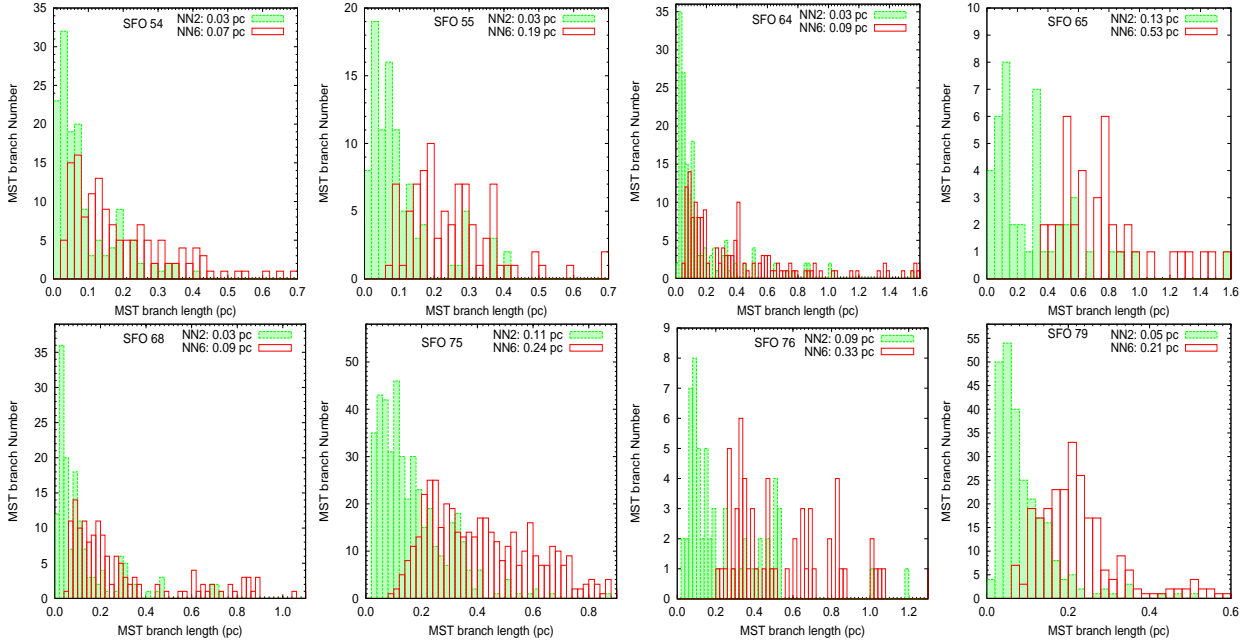


Fig. 9.— Histograms of the nearest neighbor (NN) lengths for the YSOs in the studied regions with a bin size of 0.02 pc. The red and green histograms represent NN6 ( the projected distance from each YSO to its fifth nearest YSO neighbor) and NN2 (the projected distance from each YSO to its nearest YSO neighbor), respectively (see the text for detail).

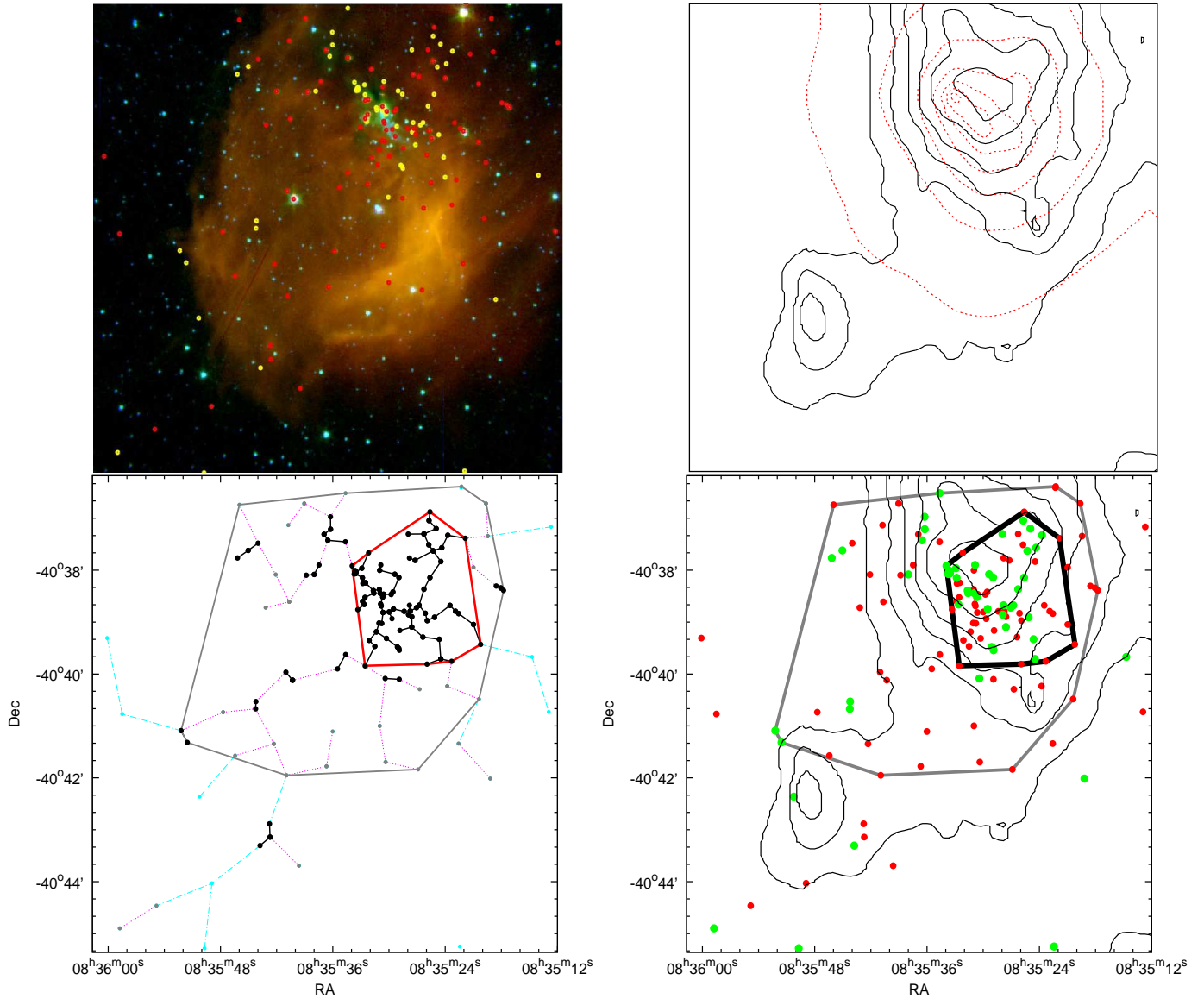


Fig. 10.— (Top Left) Color-composite image of the SFO 54 region obtained by combining the  $K$  (blue);  $3.6 \mu\text{m}$  (green) and  $8.0 \mu\text{m}$  (red) images for an area of  $\sim 10 \times 10 \text{ arcmin}^2$ . The identified YSOs (Class I: yellow dots, Class II: red dots) are also plotted. (Top Right): Isodensity contours for the YSO distribution (red dotted contours) and the reddening map (black solid contours) for the same region. The contour levels are the same as in Fig. 8. (Bottom Left): Minimal spanning tree (MST) for the identified YSOs in the same region along with the convex hull. The black dots connected with solid lines and grey dots connected with purple dotted lines are the branches smaller than the critical length for the cores and the active region, respectively. The identified core and the active region are encircled with red and grey solid lines, respectively. (Bottom Right): Spatial correlation between the molecular material inferred from the extinction map (thin black contours) and the distribution of YSOs along with the identified cores and active regions (thick black and thin grey lines, respectively).

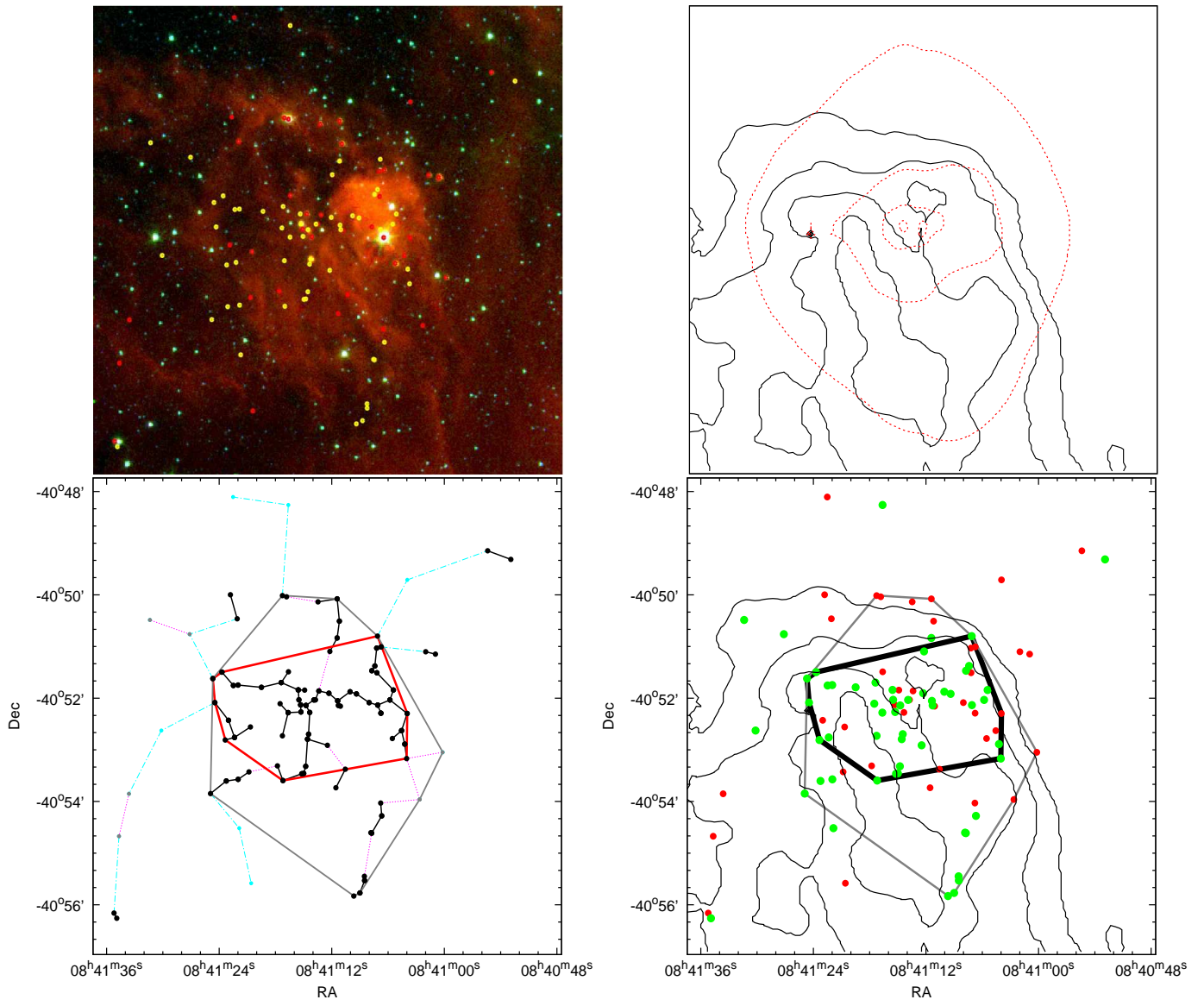


Fig. 11.— Same as Fig. 10, but for SFO 55.



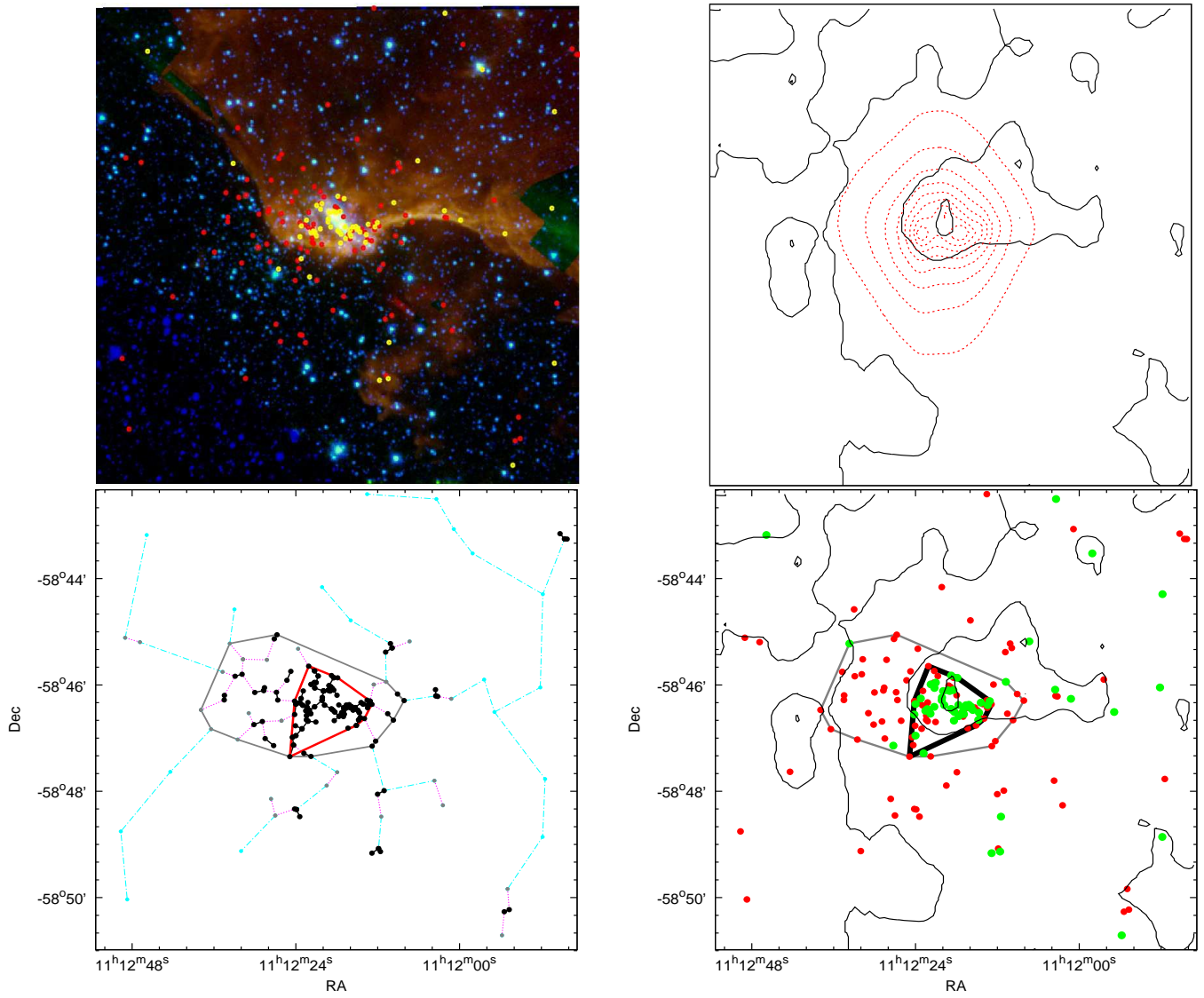


Fig. 12.— Same as Fig. 10, but for SFO 64.

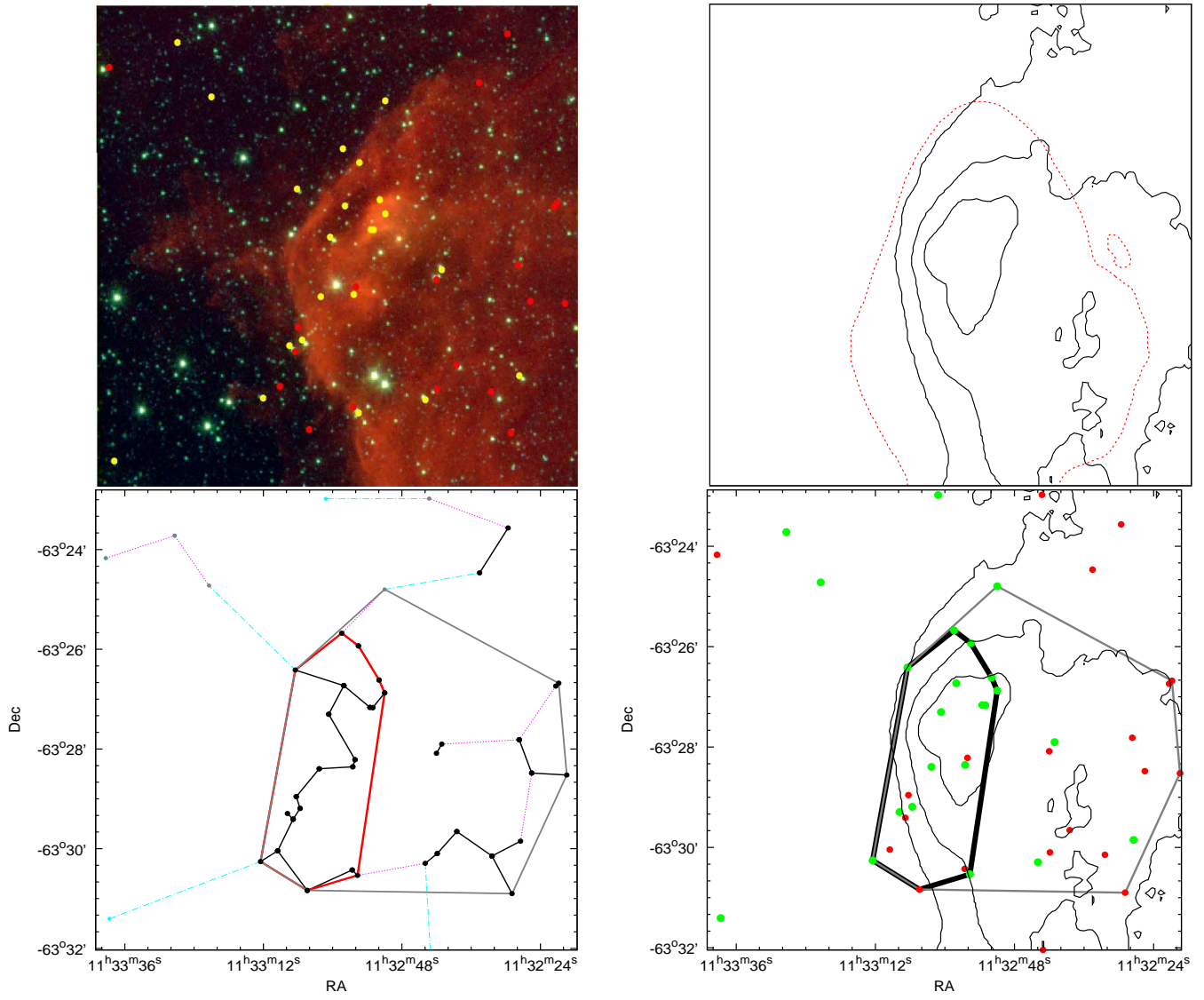


Fig. 13.— Same as Fig. 10, but for SFO 65.

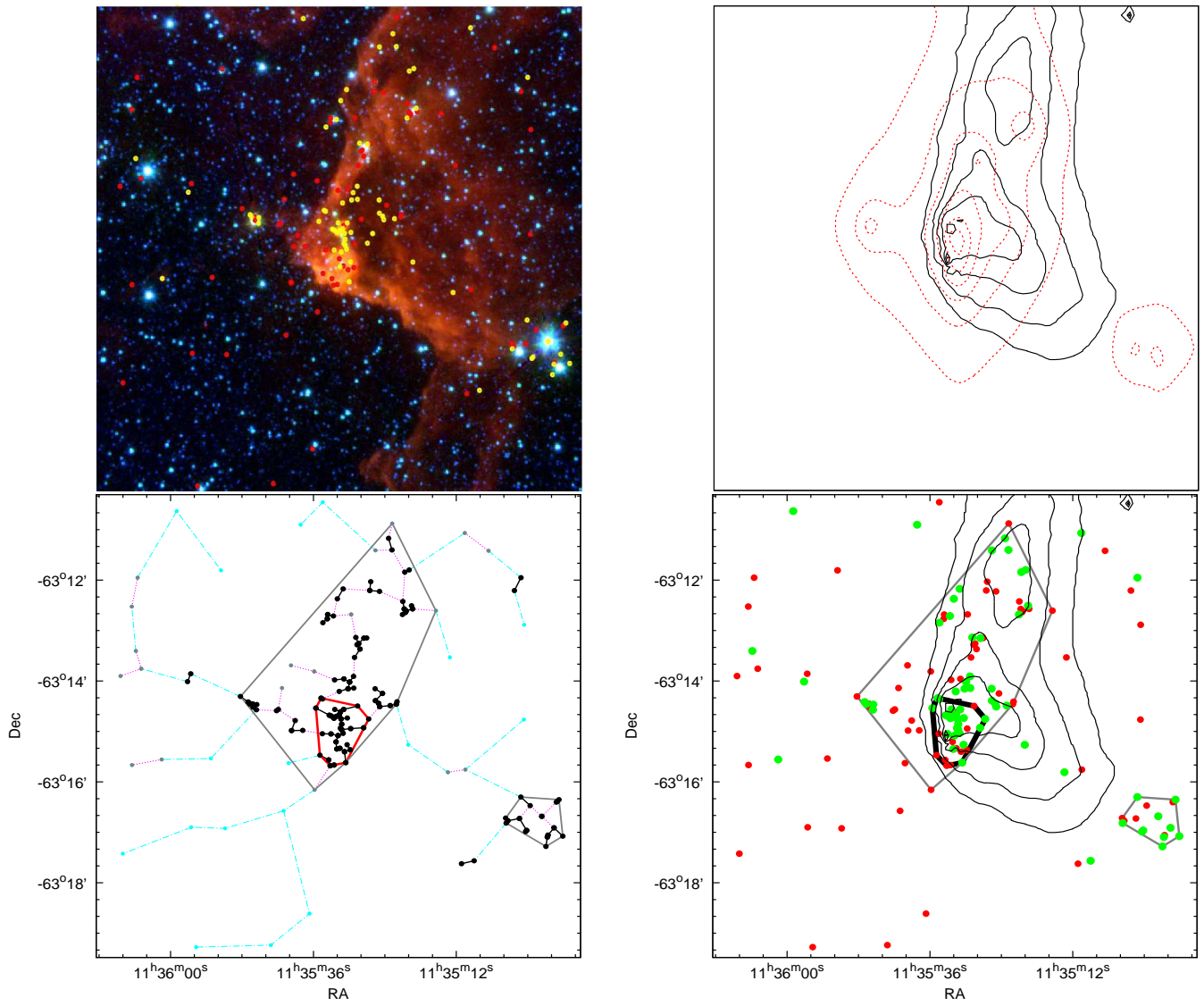


Fig. 14.— Same as Fig. 10, but for SFO 68.

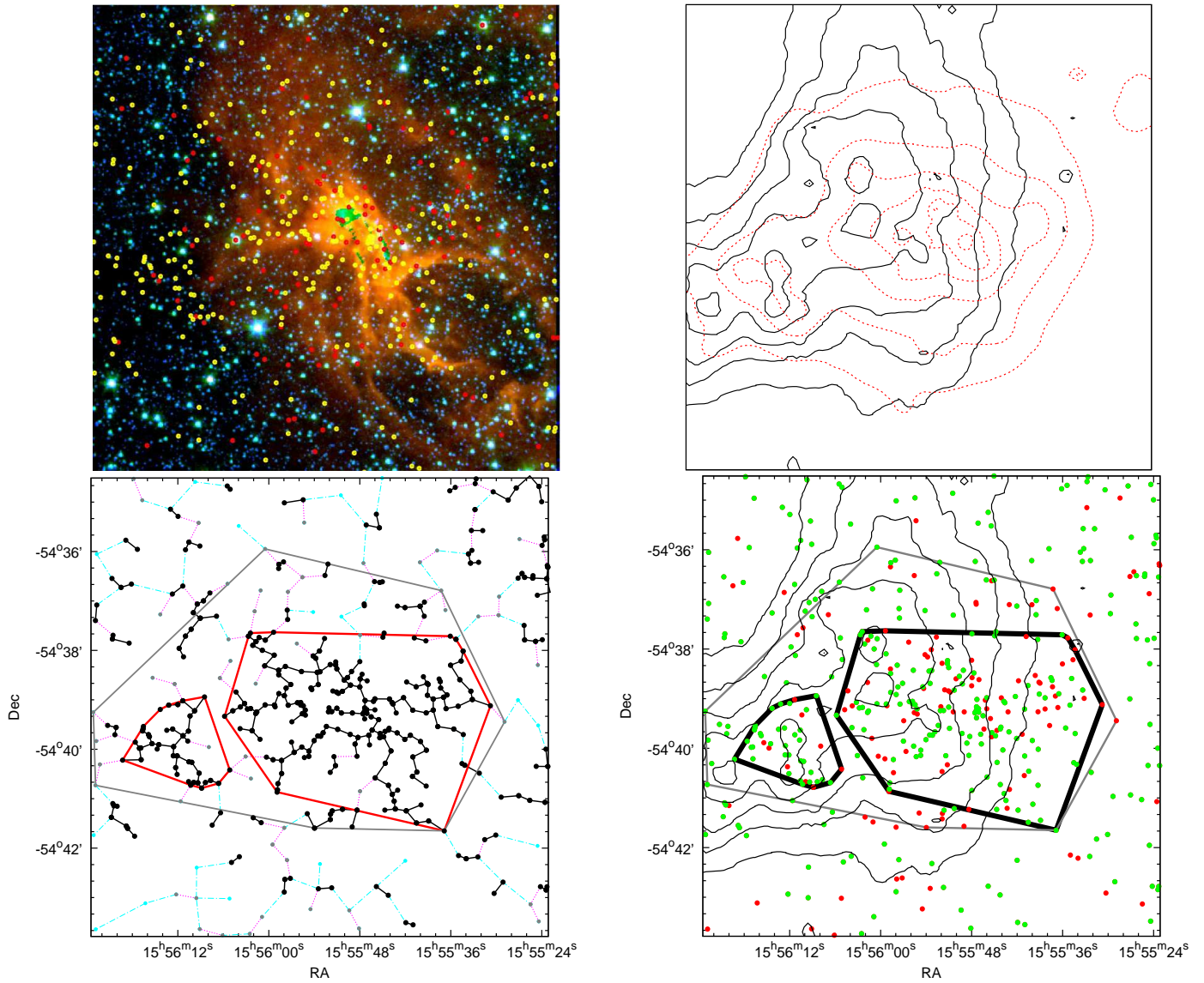


Fig. 15.— Same as Fig. 10, but for SFO 75.

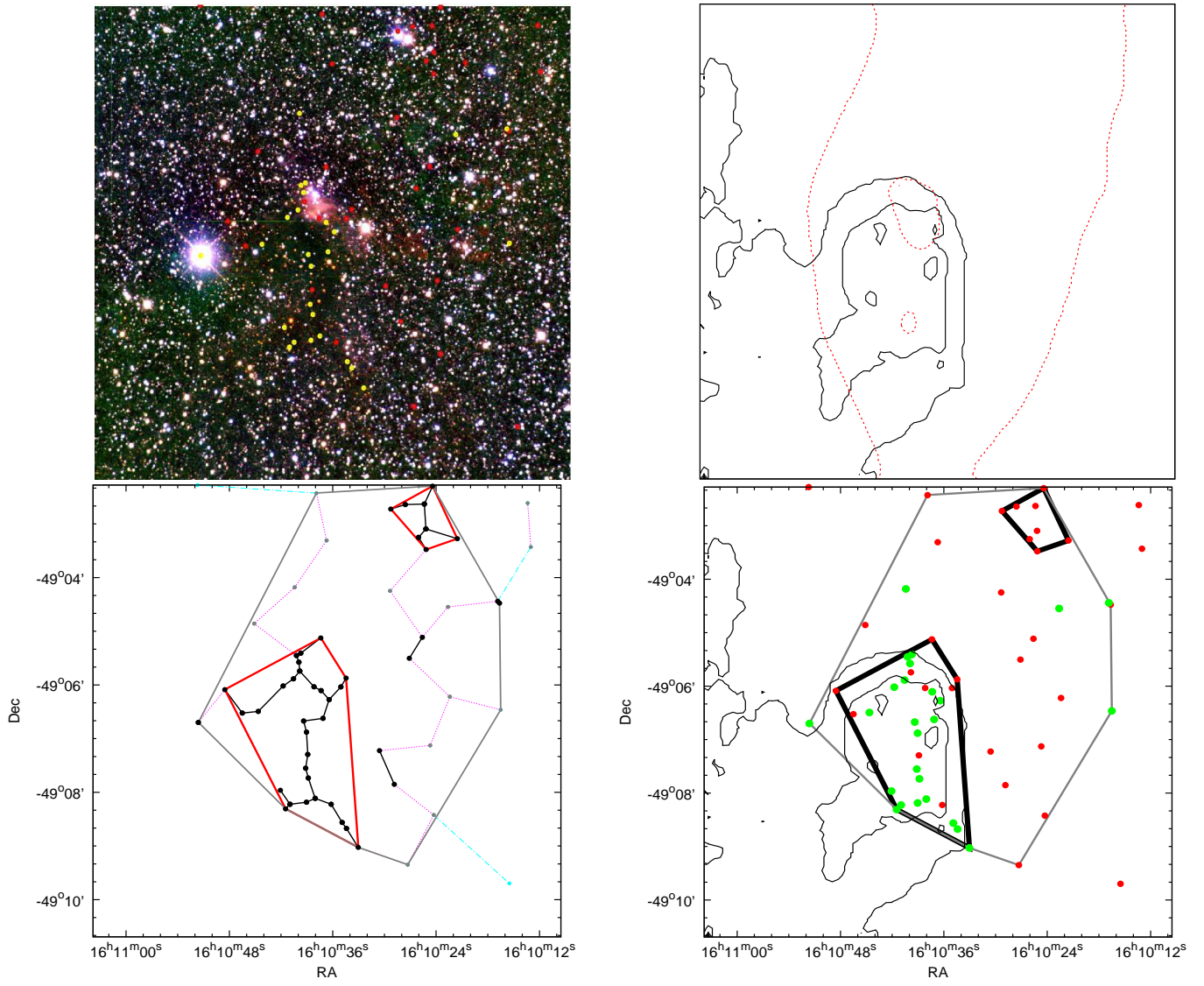


Fig. 16.— Same as Fig. 10, but for SFO 76.

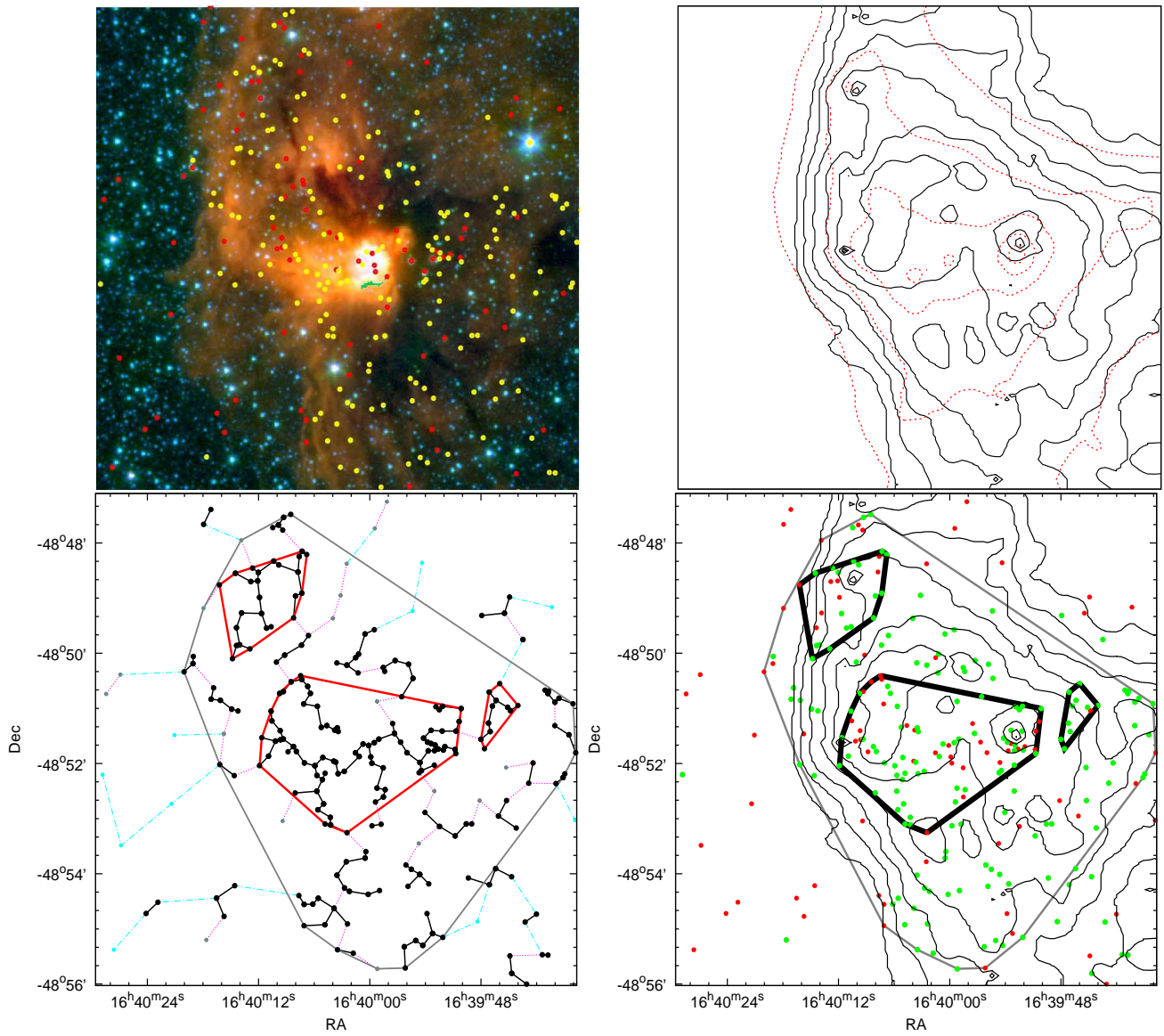


Fig. 17.— Same as Fig. 10, but for SFO 79.

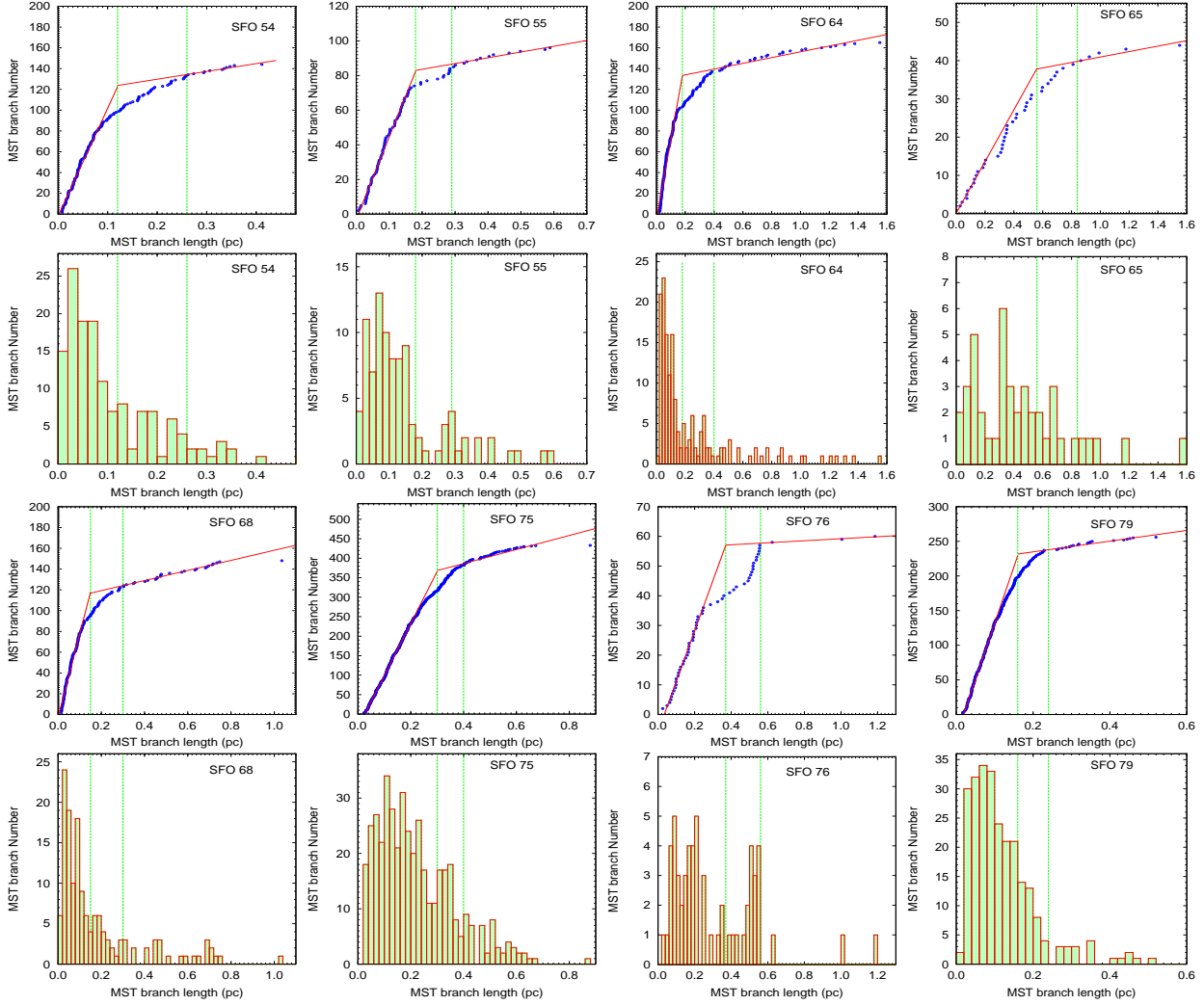


Fig. 18.— Cumulative distribution functions (CDFs) and histograms of MST branch lengths used for critical length analyses of the YSOs. The CDF plots have sorted length values on the horizontal axis and a rising integer counting index on the vertical axis. The red solid line is a two-line fit to the CDF distribution. The inner and outer vertical green lines stand for critical lengths obtained for the core and the active region, respectively.

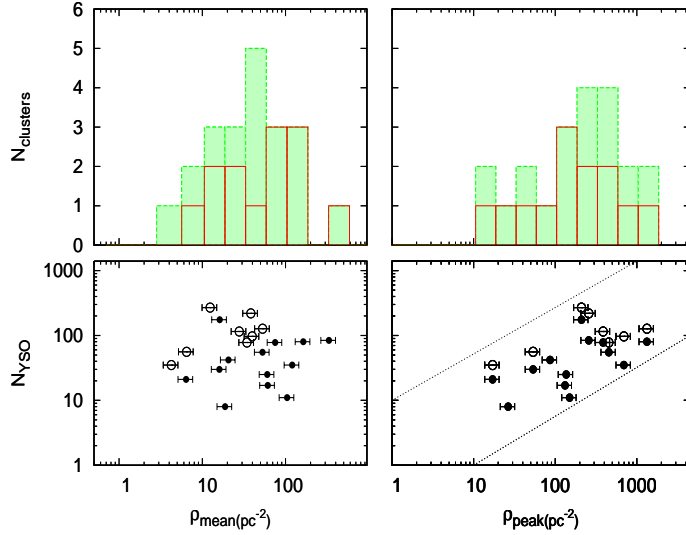


Fig. 19.— Histogram showing the mean YSOs surface density (Upper Left Panel) and the plot of the mean YSOs surface density versus the number of cluster members (Lower Left Panel). The red solid histogram and filled circles are for the cores, and the green dotted histogram and open circles are for active regions. (Right Panels): Same as Left, but for the peak YSOs surface density distribution. Dotted lines in the lower-right chart enclose all the regions with a slope of 0.8 as given in Chavarría, Allen, Brunt et al. (2014).

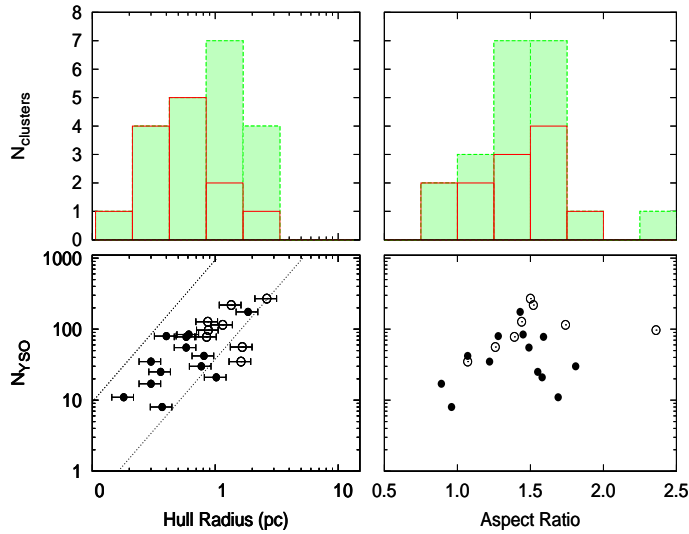


Fig. 20.— Histogram showing the hull radius distribution (Upper Left Panel) and the plot of the hull radius versus the number of cluster members (Lower Left Panel). The red solid histogram and filled circles are for the cores, and the green dotted histogram and open circles are for active regions. The dotted lines in the lower-left panel represent the constant surface densities at 12 and 300  $\text{pc}^{-2}$ . Those correspond to the range spanned by the embedded clusters from Gutermuth, Megeath, Myers et al. (2009). (Right Panels): Same as Left, but for the aspect ratio distribution.



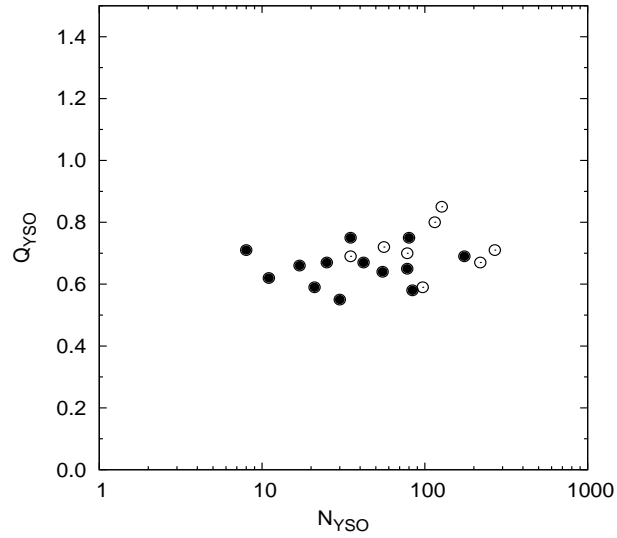


Fig. 21.— Structural  $Q$  parameter ( $Q_{\text{YSO}}$ ) for the YSOs in the cores (filled circles) and in the active regions (open circle).

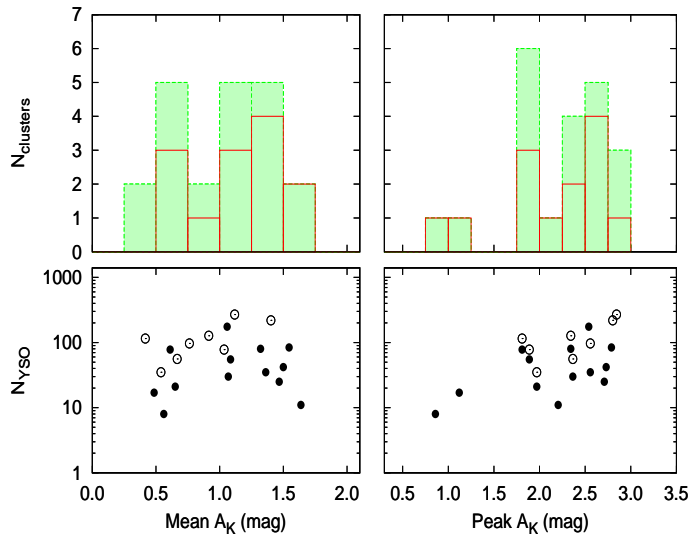


Fig. 22.— Histogram showing the mean  $K$ -band extinction (Upper Left Panel) and the plot of the mean  $K$ -band extinction versus the number of cluster members (Lower Left Panel). The red solid histogram and filled circles are for the cores, and the green dotted histogram and open circles are for active regions. (Right Panels): Same as Left, but for the peak  $K$ -band extinction distribution.

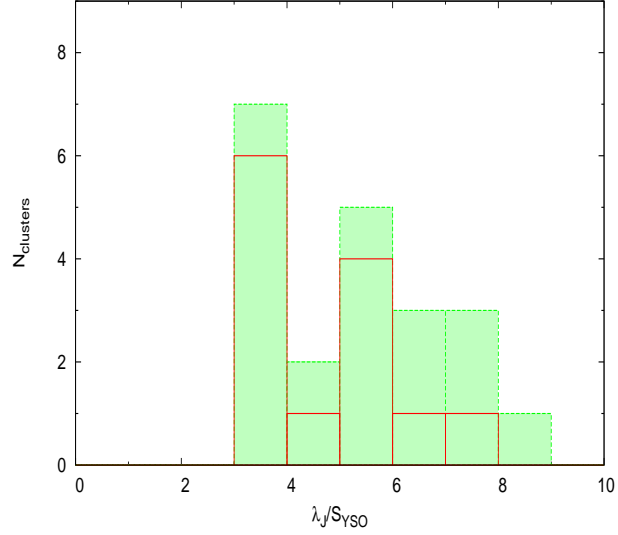


Fig. 23.— Histogram showing the distribution of the ratio between the cluster Jeans length ( $\lambda_J$ ) and the mean projected distance between the members of cores and active regions. The red solid histogram is for the cores, and the green dotted histogram is for active regions.

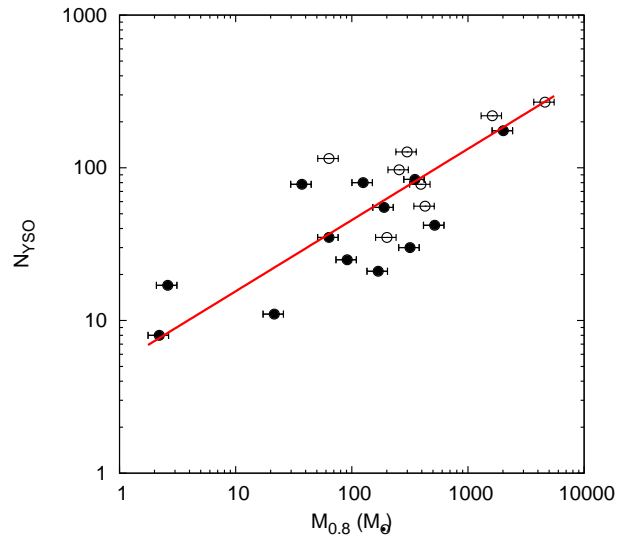


Fig. 24.— Relation between the number of YSOs ' $N_{YSO}$ ' and the molecular mass above  $A_K = 0.8$  mag ( $M_{0.8}$ ) in the cores and the active regions. The solid line shows the best fit to the data points.

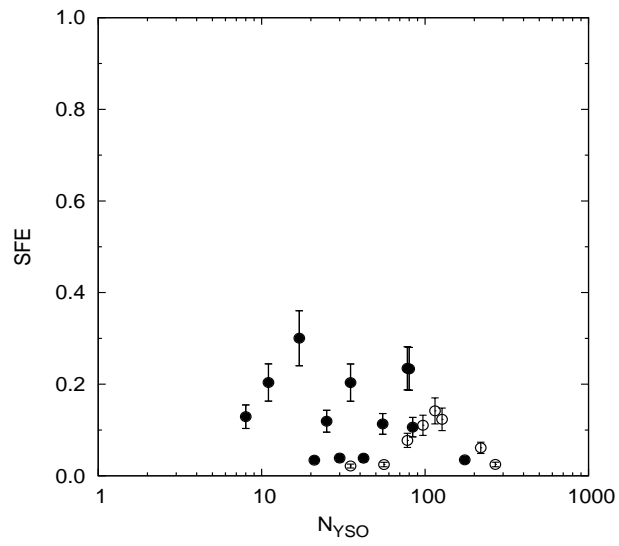


Fig. 25.— Star formation efficiency in the cores (filled circles) and in the active regions (open circles) with respect to the number of YSOs ' $N_{YSO}$ '.